Lund University, Faculty of Engineering

in collaboration with IBM Research Zurich

Master's thesis

Integration of III-V light sources for silicon photonics applications

Author:
Louise Laurenius

Supervisors:
Dr. Sepideh Gorji Ghalamestani
Dr. Lukas Czornomaz
Dr. Stefan Abel

May 11, 2016

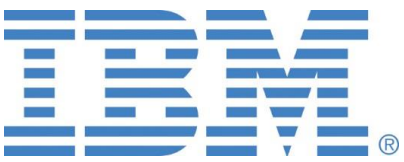

Lunds universitet
Lunds Tekniska Högskola

Abstract

During the last decades, there have been tremendous improvements in Silicon-based transistor technologies such as operational speed increase as well as size and cost reduction. However, the bandwidth in modern processors is significantly limited by the data transfer in the metallic interconnects. Inspired by the long-range telecommunication technologies, the industry is developing the field of integrated optics to transfer data in the pursuit to reach higher bandwidths. A promising approach is using a complementary metal oxide semiconductor (CMOS) compatible with silicon photonics platform. In order to outperform the conventional metallic interconnections, there is a great need for electro-optical components. Up to date, a highly efficient on-chip light source integrated on silicon is missing to complete the full optical link.

This thesis aims to design and fabricate a lateral current injection laser integrated on silicon. Optical simulations were conducted to define the parameter space for which a low lasing threshold could be achieved. Prior to the laser fabrication, the passive components of the laser including access waveguides, grating couplers and Bragg reflectors, were separately fabricated and evaluated to ensure their performance. A gain material based on an epitaxially grown multiquantum well stack with an emission peak at 1288nm was successfully integrated on a silicon oxide layer on a silicon substrate. The laser designs were patterned by a wet etch process and the effect of surface preparation prior to the contact regrowth was studied in detail. These results have contributed to a solid establishment of the initial processing steps for the realization of LCI lasers integrated on IBM's silicon chips in the near future.

Contents

Abstract **iii**

1 Introduction **1**
1.1 Motivation 1
1.2 Laser background 3
1.3 State of the art lasers for photonic integrated circuits 3
1.4 Design concept and project aims 5

2 Theory **9**
2.1 Multiquantum-well laser 9
2.1.1 Gain material 9
2.1.2 Optical resonator 10
2.2 Laser operation 11
2.2.1 Optical amplification 12
2.2.2 Lasing threshold 13
2.3 Optical mode propagation 15

3 Device design **17**
3.1 Optical simulations 18
3.1.1 Investigation of quantum well width dependence 19
3.1.2 Investigation of contact recess depth and quantum well width dependence 21
3.1.3 Effect of doping level 22
3.2 Contact resistance versus losses 23
3.3 Laser performance estimation 24
3.4 Summary of device design 25

4 Active devices **27**
4.1 General process concept 27

4.2 Epitaxial growth of the multiquantum well stack . . . 29
4.3 Wafer bonding . . . 30
4.4 Regrowth masking . . . 31
4.5 Active material etching . . . 33
4.6 Epitaxial contact regrowth . . . 34
4.6.1 Investigation of surface preparation . . . 35
4.6.2 Transmission electron microscopy analysis . . . 37
4.6.3 Active samples . . . 39
4.7 Summary of active devices . . . 41

5 Passive devices **43**
5.1 Material choice and device fabrication . . . 43
5.2 Fiber optical measurement setup . . . 44
5.3 Grating couplers . . . 45
5.4 Access waveguides . . . 47
5.5 Distributed Bragg Reflectors . . . 48
5.6 Summary of passive devices . . . 50

6 Conclusion and outlook **51**

A The laser rate equations **53**

B Hall Effect Measurements **55**

C Complex effective refractive index model **57**

Acknowledgements **59**

References **61**

Chapter 1

Introduction

1.1 Motivation

It is expected that by the year 2020, there will be six devices connected to the Internet for each person on the planet [1]. The new era of "Internet of Things" has the potential to optimize our way of living but doing so it will generate enormous amounts of data which has to be processed and analyzed in real time. The vast increase in data and hence demand for higher computing power is beyond the current capacity of our modern processors and big data centers. Scaling transistors opens up the possibility to integrate a larger number of transistors on the same chip size resulting in a higher transistor density and an increased complexity of the interconnecting network in integrated circuits (ICs). Conventionally, electrical interconnections in the form of metallic wiring are used to transfer data from one place to another. The bit-rate capacity of the electrical wiring depends on the aspect ratio between the cross-sectional area and the length of the wire as it alters the RC delay [2]. In addition to higher power consumption as a result of increased resistivity, reduced dimensions also facilitate "skin effects" meaning that the current density is non-uniform across the wire which limits the band width of the device [3]. Consequently, the time delay in processors are limited by the interconnects rather than the speed of transistors [4]. To overcome the bottleneck created by scaled electrical interconnects, many researchers have taken inspiration from telecommunication technologies where photons are used (instead of electrons) to transfer information over long-range optical fibers. Unlike electrical interconnections, optical ones do not face the same scaling limits and therefore the signal attenuation could be almost negligible if design and fabrication are optimized [2, 5].

When using optics in integrated circuits, the light waves which are often referred to as optical mode(s), propagate inside so-called waveguides. A waveguide is created by having a higher refractive index material n_f, than the surrounding material n_c. Thus, light is confined and can propagate along a given direction inside the waveguide. Various designs are available such as planar and ridge waveguides, see Figure 1.1. It is the effective refractive indices of the optical modes supported by the waveguide which determine how efficiently the light propagates. The effective refractive indices are directly related to the constituent material characteristics and structural dimensions of the waveguide [6, 7]. Silicon is the principal material used in semiconductor electronics because of its desirable properties such as low resistance and possibility to operate at high temperatures in addition to its low cost.

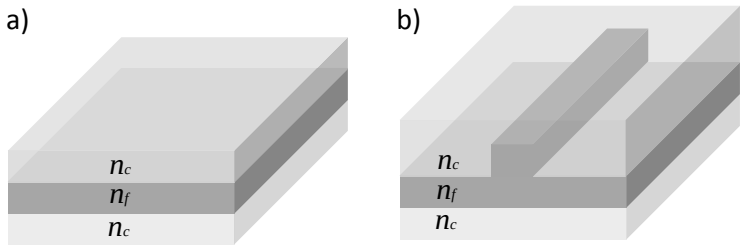

Figure 1.1: Schematic illustrations of a a) Planar waveguide and a b) Ridge waveguide where photons are confined inside a higher refractive index material n_f.

In order to establish a full optical link, integrating optical components such as modulators, detectors and light sources is essential. While detectors and modulators are close to reaching the performance needed for the optical interconnections, on-chip light sources are still a great concern. A high performance silicon light source would be ideal for integration on the silicon photonics platform, however silicon has an indirect bandgap which makes it not suitable for emitting coherent light. Despite recent advances in silicon Raman laser technology, where the amplification mechanism is based on Raman scattering which re-emits photons from the optical pumping of the laser, their performance cannot be compared to existing hybrid silicon lasers [8–13]. The hybrid silicon laser includes integration of a direct bandgap III-V light emitting source on silicon. This process has proven to be challenging due to the mismatch in lattice parameters and crystal symmetries between the III-Vs and silicon which can cause strain and defect formation in the interface between the materials. Such defects can often propagate into the structures and deteriorate their device performance. Additionally, a light source with an ultra-low power consumption is needed to be able to compete with the conventional ICs.

1.2 Laser background

Prior to designing a laser, it is essential to understand the basic physics behind light emission and how photons interact with materials. In a semiconductor, incoming photons can interact with atoms that are either in their ground state or excited state. The principle of a laser is that incoming photons interact predominantly with electrons excited to the conduction band rather than electrons exisiting in the valence band. The interaction between an incoming photon and an excited electron induce an electron-hole recombination across the bandgap under emission of a photon. The emitted photon is identical to the incident photon, they are coherent with each other, meaning that they have the same energy, phase and direction. The process is called stimulated emission and contributes to optical amplification, also referred to as gain. However, the incoming photons can also be absorbed in the material. Optical gain is obtained when the incoming photons contribute to stimulated emission more frequently than they are absorbed. To achieve this, a larger number of electrons should exist near the edge of the conduction band than near the edge of the valence band, meaning that the electron population must be inverted. An inverted population can be obtained either by optical or electrical pumping, where the latter is required for IC integration. A positive gain does not necessarily mean that a lasing mode exist. Photons produced in the material may be reabsorbed or scattered out of the gain material contributing to loss. The system reaches its lasing threshold only when the gain exceeds the losses. More details are given in Chapter 2.

1.3 State of the art lasers for photonic integrated circuits

Today, most commercially available silicon photonic chips function based on coupling light from external sources. However, to create an efficient short range optical link, an on-chip laser light source is needed. The integration of on-chip III-V lasers have up until now been focused on designs having the contacts situated above and below the active region, so-called vertical current injection (VCI) lasers, see Figure 1.2 a). In order to create an ultra-low power consumption laser, a more flexible and efficient laser design needs to be developed where the optical mode overlaps with the active region to a high degree. When the mode overlaps with the material in the doped contact regions, free carrier absorption is induced which minimizes the possibility for the device to reach a lasing mode. A. Furuya et. al. [14] suggest that it is possible to decrease the overlap of the optical mode with the contact regions ten times if a lateral current injection (LCI)

multiquantum well (MQW) structure is adopted, see Fig 1.2 b).

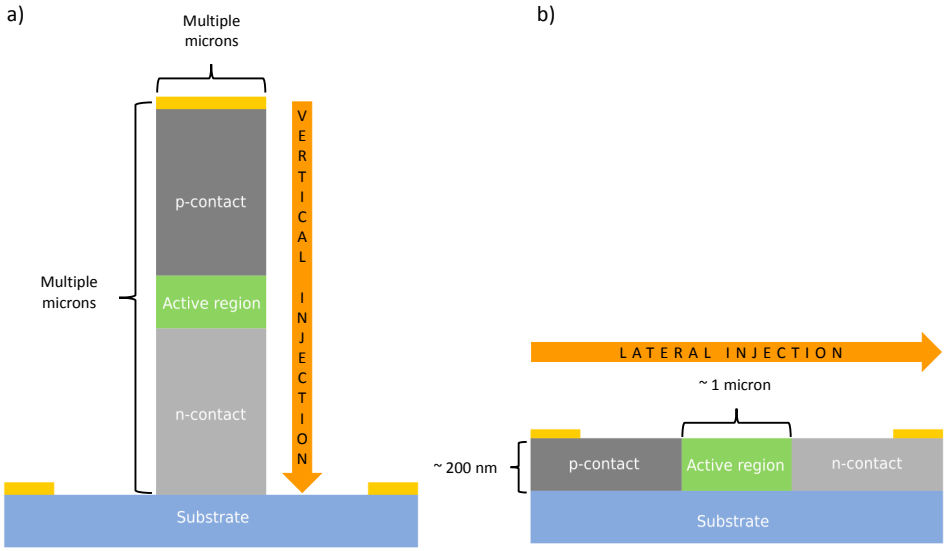

Figure 1.2: Schematic illustrations of the cross-sections of a) a vertical current injection (VCI) laser and b) a lateral current injection (LCI) laser.

In the LCI design, the thickness of the active region is only a couple of hundred nanometers leading to very high confinement of the optical mode in the vertical direction. The increased overlap of the optical mode and the active region decreases the free carrier absorption and threshold current, leading to an increased power efficiency. Additionally, the directions of current injection and highest confinement of the optical mode are orthogonal making it possible to partially decouple the two parameters when designing the structure [14, 15]. Another advantage with the LCI design is that injecting current laterally into the QWs would in principle not be affected by the barrier thickness between the QWs, which is the case in the vertical design [14, 16]. Although research has shown that the thermal resistance in the LCI lasers is higher than VCI lasers, the self-heating has a small effect on the lasing characteristics at low current operation [17]. In Figure 1.3, we have compared the previously reported threshold currents of selected state of the art electrically pumped MQW lasers integrated on a semi-insulating substrate. A wide spread in performance of the lasers is shown. However, the performance of the LCI lasers have the potential to be at least comparable with the VCI lasers.

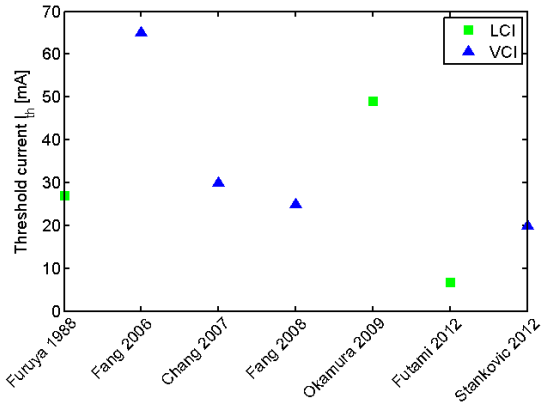

Figure 1.3: Comparison of a selection of previously reported threshold currents of electrically pumped lasers integrated on a silicon substrate.

1.4 Design concept and project aims

In this thesis, the focus has been to design a laser that is compatible with existing IBM developed CMOS technology as well has having the potential to operate at low currents. Figure 1.4 schematically illustrates the front end of line integration of the CMOS modulated laser optically coupled to silicon photonics. In order for the laser to be compatible with IBM's standard back end of line, the laser thickness is restricted to 400nm [18]. The VCI lasers have proven to be complicated to combine with the CMOS technology because of the total thickness of the structure being several microns, hindering the design flexibility. The LCI lasers on the other hand, can easily be adjusted to fit with the surrounding devices and be fabricated within the thickness budget of 400nm.

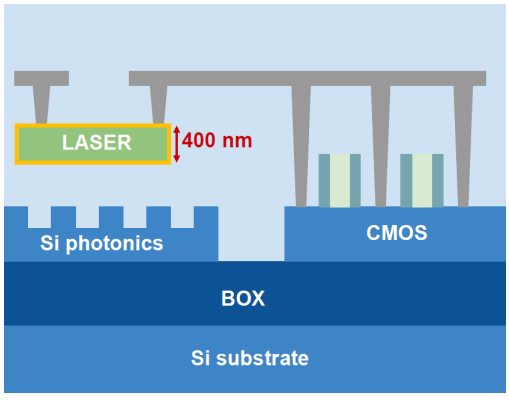

Figure 1.4: Schematic illustration of the IBM compatible the front end of line showing a CMOS modulated laser source optically coupled to silicon photonics.

It should be noted that the potential improvements associated with the development of the LCI lasers make their fabrication process rather complicated. For instance, after the patterning of the active material waveguides, the n- and p-doped contact regions need to be epitaxially regrown in two different steps. Additionally, a more sophisticated epitaxial layer stack with a seed layer incorporated for the regrowth need to be developed. The process not only includes two additional electron-beam lithography steps but also increases the risk of impurity accumulation on the side walls of the active material waveguide possibly affecting the current injection and generation of surface recombination [14]. Due to the difference in carrier mobility and refractive index of the heavily n- and p-doped contacts, a non-uniform gain and mode profile are also expected. The first generations of "bulk "LCI lasers fabricated in the late 1980's had issues with current leakage [15]. With the development of MQW LCI lasers, the current leakage problem has been reduced but cannot be regarded insignificant even in state of the art lasers [11, 19]. It has been demonstrated that a laser with improved thermal stability can be achieved by using InAlGaAs quaternary alloy as the gain material instead of InGaAsP alloy [20, 21]. The reason for choosing quaternaries for the gain material is clarified in Chapter 2, section 2.1.1.

To form a laser, other components than the active material are needed. The top view schematic of our laser, seen in Figure 1.5 a), shows the passive components; access waveguides, grating couplers and Bragg reflectors. The constituent materials and rough dimensions of the cross-section of the device is illustrated in Figure 1.5 b). The concept for our active material relies on an epitaxially grown MQW stack where 10 QWs consisting of quaternary $In_{0.64}Al_{0.13}Ga_{0.23}As$ alloys are separated by 11 $In_{0.47}Al_{0.3}Ga_{0.23}As$ barrier layers. The MQW stack is sandwiched between two $In_{0.53}Al_{0.30}Ga_{0.17}As$ buffer layers and thin layers of InP, see Figure 1.5 c). The complete epitaxial stack is integrated on a silicon oxide layer on a silicon wafer through direct wafer bonding.

Consequently, the aim of this master project is to design and fabricate a multiquantum well lateral current injection laser integrated on silicon. To accomplish this, the following points will be addressed:

- Optical simulations of the 2D cross-section of the device in order to understand what range of dimensions our laser should have to meet the requirements, covered in Chapter 3.
- Process development, covered in Chapter 4.
- Fabrication of active and passive devices, covered in Chapter 4 and Chapter 5.

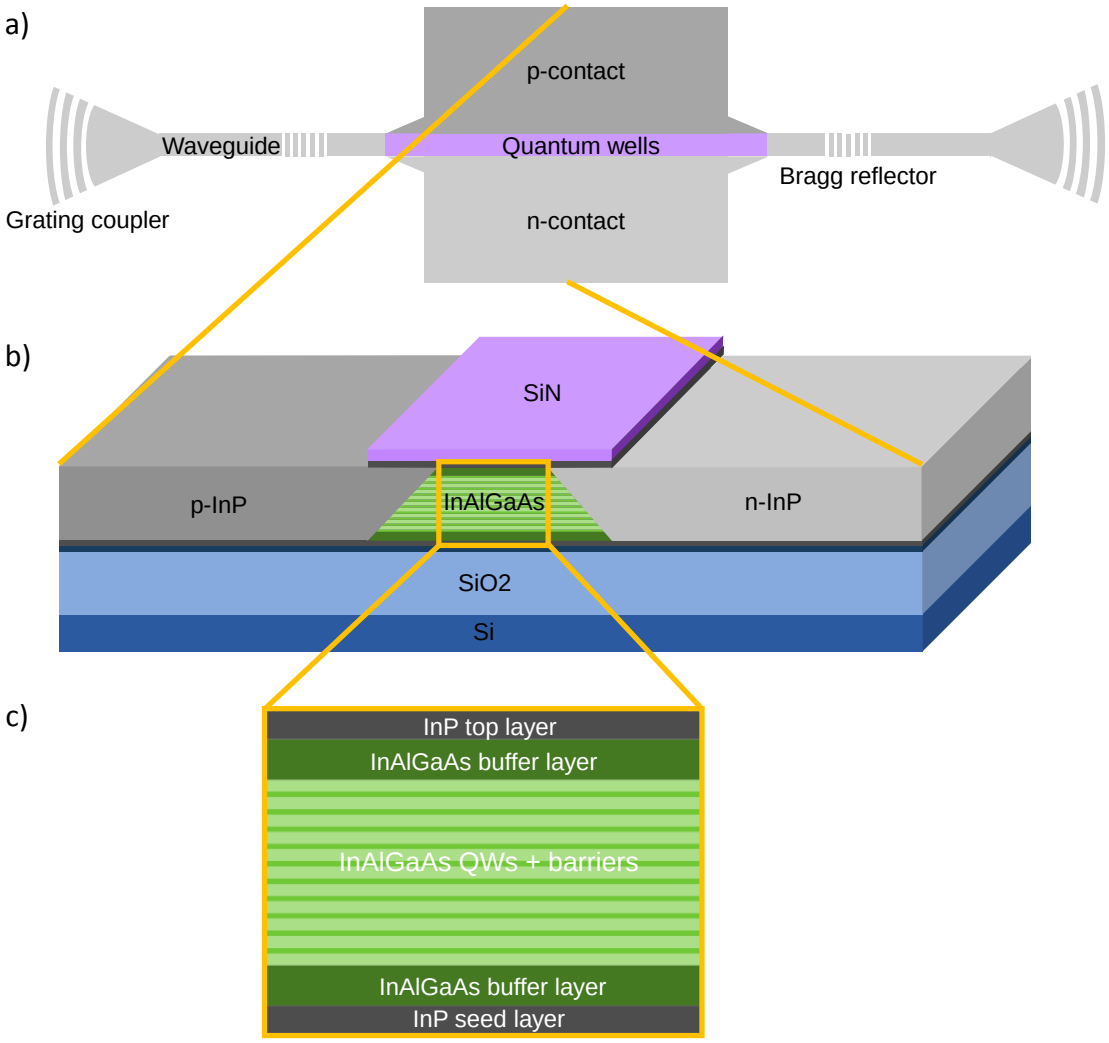

Figure 1.5: Schematic illustration of our LCI laser design where a) is a top view of the full laser including the active material (quantum wells), the n- and p-doped contacts, the access waveguides, the grating couplers and the Bragg reflectors. b) Illustrates the cross-section of the device with the constituent materials and c) illustrates the epitaxial layer stack.

Chapter 2

Theory

2.1 Multiquantum-well laser

A gain material and an optically resonating structure are the basic components of a laser. Details on the requirements of the gain material and the optical cavity are given in section 2.1.1 and section 2.1.2 respectively.

2.1.1 Gain material

In a multiquantum well (MQW) structure, the quantum well material is sandwiched between a barrier material which has a larger band gap, as shown in Figure 2.1 The energy levels in a quantum well are not continuous but quantized into a number of discrete sub-bands. It is possible to alter the band structure of the quantum well by varying the composition and/or magnitude of strain (in this case compressive strain) between the layers. The magnitude of the strain can change for instance by changing the thickness of the quantum well. Thus, it is possible to control the energy of the emitted photons [6].

When applying a bias, charge carriers are injected and confined in the wells increasing the probability of recombination occurring between specific energy levels, as shown in Figure 2.1. If the difference in lattice constants between the quantum well and barrier materials is large, the interfacial strain could become substantial and defects may be induced. The presence of defects generates unwanted carrier recombination resulting in loss of carriers contributing to the optical gain in the active material. Independent of the material composition, very thin layers can in general tolerate a relatively large amount of strain without forming defects [22]. Because the barrier material has larger bandgap, photons emitted from the quantum well are not absorbed in the barrier. Quaternary alloys are suitable materials for MQW structures because the composition can easily be adjusted to independently optimize their lattice parameter and energy bandgap. In our

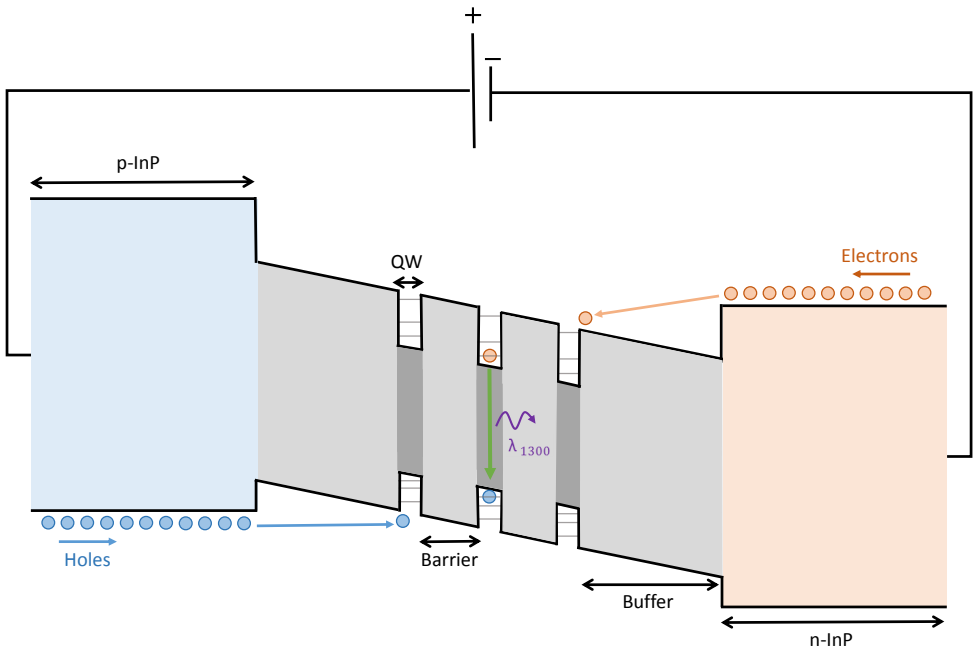

Figure 2.1: Schematic of the band diagram of vertical multiquantum well structure. The band gap of the QWs is smaller than the band gap of the surrounding barrier layers. Consequently, the charge carriers are captured in the QWs when a bias is applied. By varying the width of the QWs it is possible to control the quantized energy levels thus the energy of the emitted photons.

case, the gain material will be grown on a InP seed layer which has a lattice parameter of 5.8687 Å. By fixing the lattice parameter of the layers to approximately 5.8687 Å, the energy bandgaps of the different layers can be altered to form a multiquantum well structure.

2.1.2 Optical resonator

In addition to the gain material, a resonating structure is needed to form a laser. Inside a resonator, specific resonant frequencies are supported by the waveguide. As the resonant frequencies are reflected back and forth inside the resonator and interfere with each other, a standing wave (also referred to as optical mode) forms and an optical cavity is created. Reflection of resonant frequencies can be achieved by placing reflectors on either side of the gain material to confine the light inside the cavity. Bragg's law of diffraction describes the basics behind reflection of a plane wave between reflectors spaced at at distance d from each other:

$$m\lambda = 2d\sin\theta \tag{2.1}$$

where λ is the optical wavelength, θ is the angle between the incident ray and the reflector and m is a positive integer. Assuming a reflection straight back (180°) into the active material is desired, the Bragg relation can be adapted to the specific case. By letting d be equal to the grating period Λ, θ be equal to 90°and λ be equal to λ_0/n_g where λ_0 is the wavelength in vacuum and n_g is the effective refractive index of the optical mode, the Bragg relation is modified to:

$$2\Lambda = m(\lambda_0/n_g) \tag{2.2}$$

The reflection of the first order optical mode of a fixed wavelength and can thus be altered by the grating period [22, 23].

A high amount of reflection can be achieved by using a mirror grating concept called Distributed Bragg Reflector (DBR). The DBR concept is based on a periodic alternation of two different refractive index materials in the direction of propagation of the optical mode. At each boundary, a certain amount of light will be reflected back. Constructive interference of the reflected light for a range of frequencies around the so-called Bragg frequency, i. e. bandwidth, occurs only if the optical path length corresponds to m times half the wavelength. For wavelengths which are not within the bandwidth limits, the reflections will interfere destructively and cancel each other out. By adding N multiples of alternating index pairs, the sum of all reflections add up to a large total reflection. The total reflection R can be calculated as following:

$$R = \frac{n_0(n_2)^{2N} - n_s(n_1)^{2N}}{n_0(n_2)^{2N} + n_s(n_1)^{2N}} \tag{2.3}$$

Where n_0 is the index of the originating gain material, n_1 and n_2 are the indices of the alternating materials and n_s is the index of the terminating material [22, 24].

2.2 Laser operation

The background of laser operation was briefly introduced in Chapter 1, section 1.2 but will be explained more in this section. The principle theories behind optical amplification and the laser threshold are described in section 2.2.1 and section 2.2.2.

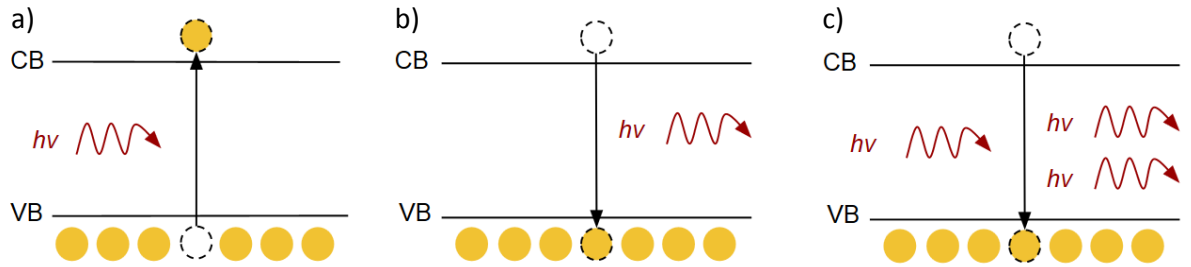

Figure 2.2: a) An incoming photon is absorbed in the material during excitation of an electron from the valence band to the conduction band. b) A photon is emitted due to electron-hole recombination without any external stimulation (spontaneous emission). c) An incoming photon interacts with an already excited electron under emission of a clone photon (stimulated emission).

2.2.1 Optical amplification

Single atoms have discrete energy levels occupied by electrons and when such atoms are brought together in form of a solid material, the energy levels become dense and form continuous energy bands. The upper energy band filled by electrons is called the valence band. The allowed energy band above the solid chemical potential at 0 K (Fermi level) is called the conduction band. The separation between the maximum level of the valence and the minimum level of the conduction band is defined as the band gap. As briefly mentioned in Section 1.2, photons interact with atoms in different ways depending on the state of the atom. If the solid material system is in its ground state, an incident photon can be absorbed in the material by exciting an electron from the valence band to the conduction band and hence generating an electron-hole pair, as shown in Figure 2.2 a). As the system strives towards lowering its overall energy, the electron will eventually return to its lower energy state (valence band). During the recombination of the electron and hole, a photon is emitted with an energy or wavelength corresponding to the band gap. If the recombination occurs without external stimulation, the emission is called spontaneous emission and the emitted photon has a random direction without any correlation to the incident light field, as shown in Figure 2.2 b). The produced light is incoherent and will be seen as amplifier noise. However, if a photon with roughly the same energy as the bandgap interacts with an already excited electron, stimulated emission occurs, as shown in Figure 2.2 c). The process generates two identical photons with the same energy, phase and direction. Coherent light is produced and the two photons have the possibility to stimulate emission of another two photons.

The rate at which stimulated emission occur is proportional to the number of electrons existing in the conduction band. Optical amplification occur only if the incident photons

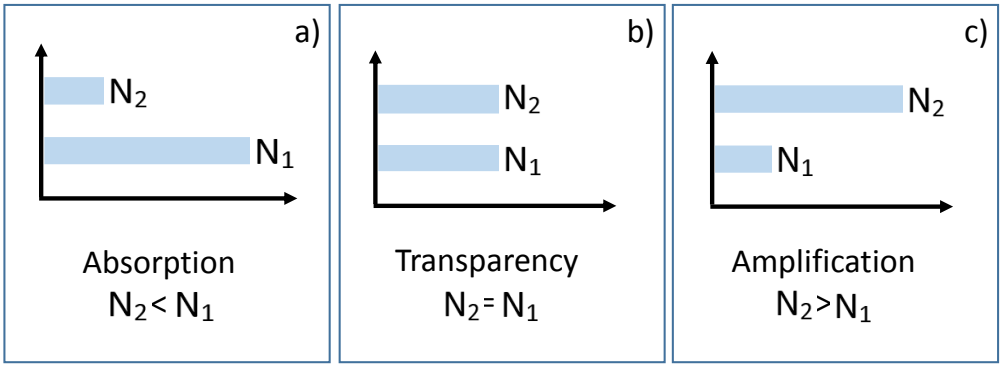

Figure 2.3: N_1 and N_2 correspond to the number of electrons in the valence and conduction band respectively. a) Absorption dominates when $N_2<N_1$. b) The material becomes transparent when $N_2=N_1$. c) Optical amplification occurs when $N_2>N_1$.

contribute to stimulated emission more frequently than they are absorbed. Therefore, the number of electrons in the valence band N_1, and in the conduction band N_2, determine the number of photons which can be gained and contribute to lasing. As long as $N_2<N_1$, the gain is negative and absorption dominates (Figure 2.3 a) but at $N_2=N_1$ the threshold is reached and the material becomes transparent (Figure 2.3 b). For $N_2>N_1$ the population is inverted, gain is positive and emission dominates. Thus, the material can act as an amplifier, (Figure 2.3 a). An inverted population can be generated by external supply of energy, either by optical or electrical pumping [6].

2.2.2 Lasing threshold

In an electrically pumped laser, carriers are injected into the conduction and valence bands when a bias is applied. From the laser rate equations, found in Appendix A, it is possible to determine the carrier density N, as a function of applied current I. At a specific threshold current I_{th}, the carrier density reaches a value where the stimulated emission is equal to the absorption i.e. the carrier density threshold $N=N_{th}$. If the current is increased above the threshold current I_{th}, initially the carrier density N increases above threshold value. After a very short delay, the stimulated emission also increases, reducing the carrier density until a new balance is reached. This feedback effect causes the carrier density to clamp at its threshold value N_{th}, and consequently the gain clamps at its threshold value g_{th}, as shown Figure 2.4. The threshold carrier density, N_{th} is given by [22]:

$$N_{th} = N_{tr} \exp\left(\frac{1}{\Gamma g_0}\langle\alpha_i\rangle + \frac{1}{L}\log\left(\frac{1}{R}\right)\right) \tag{2.4}$$

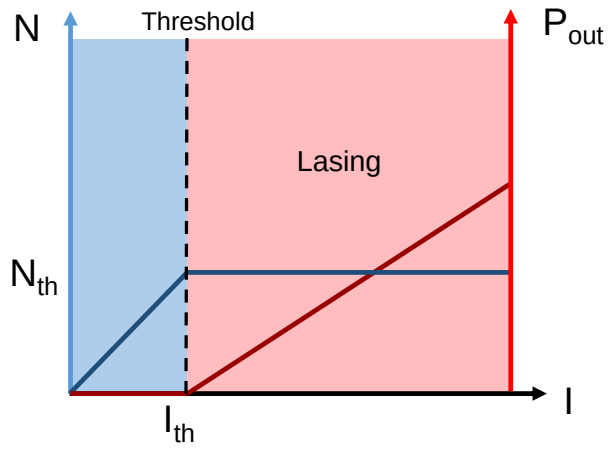

Figure 2.4: Illustration of how the carrier density N and the optical power output P_{out} change as a function of current I.

Where N_{tr} is the transparency carrier density, Γ is the modal confinement factor, g_0 is the material gain factor, $\langle \alpha_i \rangle$ is the internal losses, L is the total cavity length and $R = r_1 r_2$ is the mean mirror intensity reflection coefficient. The threshold current I_{th}, in the steady state can be obtained by calculating:

$$I_{th} = \frac{qV_{QW}}{\eta_i} B N_{th}^2 = \frac{qV_{QW}}{\eta_i} B \exp\left(\frac{2}{\Gamma g_0}\left(\langle \alpha_i \rangle + \frac{1}{L}\log\left(\frac{1}{R}\right)\right)\right) \tag{2.5}$$

Where q is the carrier charge, V_{QW} is the volume of the active material, η_i is the carrier injection efficiency and B is a bimolecular radiation coefficient [22].

In the steady state regime, when $I > I_{th}$, the carrier density and gain are clamped and the photon density N_p can be derived from the laser rate equations:

$$N_p = \eta_i \left(\frac{I - I_{th}}{v_g g_{th} V_{QW}}\right) \tag{2.6}$$

where v_g is the waveguide group velocity. The optical power output is linked to the photon density N_p and by considering the energy stored inside the cavity and the losses, the output power above threshold, P_{out}, can be calculated as a function of input current, I:

$$P_{out} = \frac{hc}{\lambda q} \eta_i \left(I - I_{th}\right) \frac{\alpha_m}{\langle \alpha_i \rangle + \alpha_m} \tag{2.7}$$

where h is Planck's constant, c is the speed of light, λ is the wavelength, q is the elementary charge, $\langle \alpha_i \rangle$ is again the internal absorption losses and α_m is the mirror losses. A schematic of the power output versus current density is illustrated in Figure 2.4.

2.3 Optical mode propagation

Light is an electromagnetic radiation consisting of synchronized oscillations of electric and magnetic fields which are perpendicular to the direction of the transverse light wave propagation, as shown Figure 2.5. The law describing the combined electric and magnetic response in a medium is summarized in Maxwell's equations of electromagnetism [6, 25], see Appendix A. Optical modes are orthogonal solutions of the electromagnetic wave equation based on Maxwell's equations and describe the propagation of light in a dielectric medium. A transverse mode is therefore an electromagnetic field pattern with it's shape determined by the boundary conditions of the specific structure.

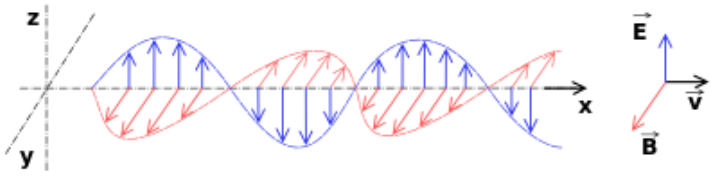

Figure 2.5: Electromagnetic wave.

The direction of the electric field in an electromagnetic wave is called polarization. Unguided electromagnetic waves, or transverse electromagnetic (TEM) modes, have neither a specific electric or magnetic field in the direction of propagation (E_x=0, H_x=0). In waveguides, the supported modes are often divided in three categories depending on their polarization:

- Transverse electric (TE), (E_x=0, $H_x \neq 0$)
- Transverse magnetic (TM), ($E_x \neq 0$, H_x=0)
- Hybrid, ($E_x \neq 0$, $H_x \neq 0$)

Depending on the geometry of the waveguide, it is possible that multiple modes of each polarization are supported by the structure. The TE and TM modes with the simplest gaussian mode profile are called *fundamental modes* and modes with a more complicated profile are referred to as *higher order modes*. Even if multiple modes are supported by the structure they do not interfere with each other and the light is only coherent within each specific mode [6, 22].

For the design of waveguides, it is important to understand that light waves traveling through a waveguide attenuates. There are three main mechanisms contributing to the loss of intensity; absorption, scattering and radiation. Absorption could be significant in

semiconducting waveguides and arises due to the interaction between photons and charge carriers in the waveguide material. Losses which arise due to change of direction of the photons out of the waveguide are caused either by scattering or radiation. Scattering of photons occur either at the surfaces due to surface roughness or inside the waveguide due to imperfections in the crystal such as grain boundaries and voids. Radiation losses depend on the confinement of the modes inside the waveguide. If the mode is poorly confined, photons will radiate out into the surrounding material [23, 26].

Chapter 3

Device design

The aim of simulating photonic waveguides is to get a full understanding of how optical modes are supported and propagate inside a specific waveguide. Ideally, only a single mode should be supported by the structure to have a narrow linewidth and low noise. For straight waveguides, a 2D cross-section eigenmode solver provides useful information about the existing modes in the specific structure. In 2D waveguides, pure TE or TM modes do not exist but instead the resulting modes are mixtures of the two polarizations. A well-known 2D eigenmode solver is the finite difference (FD) method which can solve Maxwell's equations for a specific frequency. The requirement for light to be confined inside the waveguide is that the effective refractive index (n_{eff}) of the optical mode has to be higher than the n_{eff} of the cladding but lower than the n_{eff} of the active gain material. A waveguide supporting only a single TE or TM mode is ideal but can be rather difficult to accomplish in reality. However, by simulating parameter sweeps such as the waveguide width, it is possible to determine in what dimensional range a behavior close to single mode exists. Such information helps us to know for instance "which dimensions we should use for our devices" and "what behavior we can expect from them". Additionally, the simulation results can provide information about the modal confinement (Γ), effective refractive index (n_{eff}) and absorption loss (α) values.

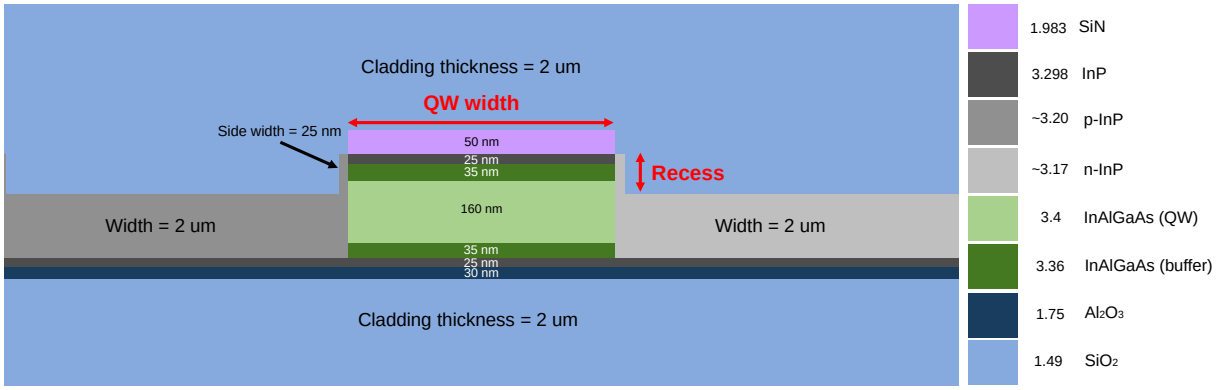

Figure 3.1: a). An schematic cross-sectional illustration of the structure used for simulation, showing thicknesses of constituent materials and corresponding refractive indices (on the right). The QW and barriers were assumed to be a single region with an average refractive index of 3.4

3.1 Optical simulations

Prior to the simulations, details of the structure such as material indices and dimensions need to be defined. Figure 3.1 shows the schematic cross-sectional illustration of the structure including thicknesses of various layers and their corresponding refractive indices. To simplify the simulations, both the QWs and barriers were assumed to be a single region with an average refractive index of 3.4. The simulation tool used was the OptoDesigner from PhoeniX Software version 5.0.7.

The refractive index is a dimensionless complex number originating from the dielectric function. The complex refractive index is composed of two parts, $\underline{n}=n+ik$, where the real part n, is the ordinary refractive index determining the phase velocity, and the imaginary part k, is the extinction coefficient determining the material absorption losses [25]. By introducing dopants, a material's conductivity changes from being a pure semiconductor to a more "metal-like" material in which the free carrier absorption is higher.

As explained in Section 2.2, the lasing threshold is reached when the modal gain exceeds the losses. Assuming infinitively straight side walls and a defect-free material, the remaining losses are associated with the degree of modal confinement in the gain material and in the contact regions. In the LCI structure, there is a large difference in the refractive index in the vertical direction but not in the horizontal direction. In our studied structure, the difference in the refractive index value between the InP contact regions and the active region is only around 0.2 and consequently the mode spreads out into the InP contacts. The goal of the optical simulation study is to maximize the overlap with the gain material and to minimize the overlap with the absorptive InP contacts in order to largely reduce the threshold current. The lateral confinement can be improved by

lowering the average refractive index of the n- and p-doped contacts in several ways such as changing the doping level, creating a photonic crystal structure or etching a recess. By etching a recess, parts of the contact material is removed and replaced with the cladding material which has a lower refractive index. Increasing the doping level decreases the index, however this would also increase the absorption losses and resulting in an unwanted increase in lasing threshold and decrease in optical output power (clarified in 3.1.3). Adopting photonic crystal structure is a promising alternative approach. Considering the time given to this project, it would be regarded as an unrealistic task since it would require many optimization steps. This leaves us with the contact recess solution which is reasonable both in terms of simulation and fabrication work.

As shown in Figure 3.1, a 25nm thin strip of InP contact material, which is the level of alignment accuracy that can be achieved by the electron-beam lithography, was kept on each side of the active region so that the electrical injection into the QWs would still be possible if the recess depth reached the QWs.

3.1.1 Investigation of quantum well width dependence

The simulations were started by investigating the affect of varying the quantum well width on modal effective refractive index, the confinement in the active region, the losses. Increasing the quantum well width allows a larger volume for the mode to be confined within and thus the modal overlap with the contacts should decrease. Since the majority of the losses originate from the contact overlap the losses should also decrease as the quantum well width increases. However, a wider structure supports a larger number of modes. In the simulations, the QW width was varied from 100 nm to 2000 nm with an interval of 100 nm and the recess was kept constant at 60 nm. The effect of the QW width on the mode size in the lateral direction of the fundamental TE mode is shown in Figure 3.2 a). The mode size is defined as twice the distance from the center to the point where the intensisty has dropped to $1/e^2$. As shown in Figure 3.2 a), the mode size changes significantly and reaches a minimum for a QW width of around 400 nm.

Numerically, there are multiple modes present in the structure even for very narrow QW widths, as shown in Figure 3.2 b). It is not possible to determine whether all modes propagate in the structure without first having a look at the confinement in the active region and the losses for each individual mode. Two criteria were defined to aid finding suitable dimensions for our devices. The first criterion makes sure that our structure supports only modes with losses less than 50 dB/cm. The second criterion selects only modes that have more than 90% overlap of the mode with twice the size of the MQW

area. Applying these criteria to the obtained solutions of the QW width simulation results in Figure 3.3. As shown in Figure 3.3 a), for QW widths between 400-750 nm only the fundamental TE mode passes the criterion. Figure 3.3 b) shows the obtained losses versus QW width and indicates that for QW widths between 500-1000 nm, only the fundamental TE mode passes the criterion.

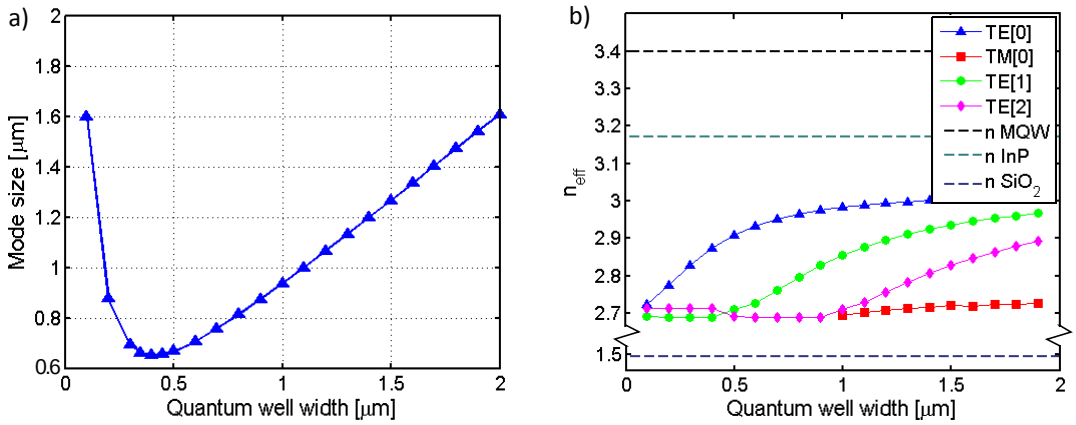

Figure 3.2: a). Simulation of the mode size of the fundamental TE mode versus the quantum well width. b) Simulation of the effective refractive index (n_{eff}) of supported modes in the quantum well versus the quantum well width.

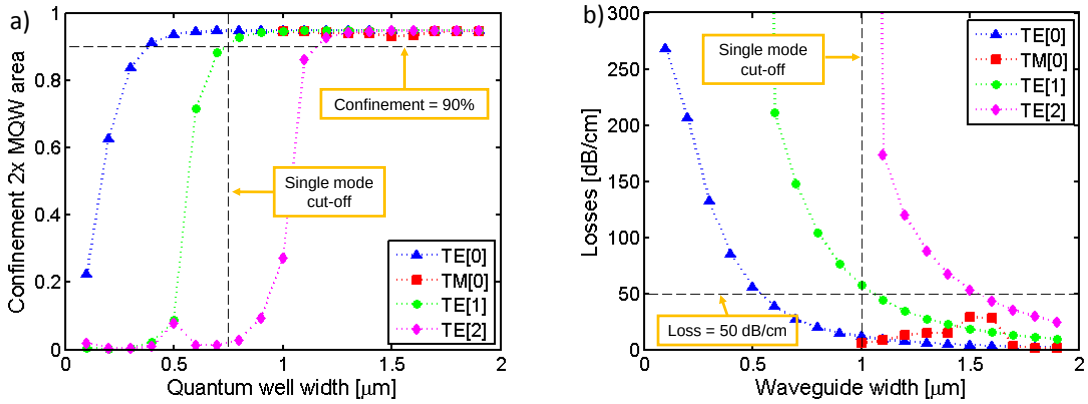

Figure 3.3: a). Simulation of the confinement in area of twice the MQW area for supported modes versus the width of the quantum well. Up to QW widths between 400-750 nm, only the fundamental TE mode passes the criterion of over 90% modal confinement in twice the size of the MQW region b) Simulation of the losses for the supported modes versus the width of the quantum well indicating that for QW widths between 500-1000 nm, only the fundamental TE mode passes the criterion.

3.1.2 Investigation of contact recess depth and quantum well width dependence

To evaluate the effect of etching a recess in the InP contacts, a simulation sweep was conducted where both the quantum well width and recess depth were varied. By etching a recess, parts of the high refractive index contact material is removed and replaced with the low refractive index cladding material. The overall contrast in refractive index between the active region and the surrounding is increased and thus the optical mode should be confined in the active region to a higher degree.

The QW width was varied in the range of 400-1000nm and the recess depth was varied in the range of 0-120nm. Maps of the losses and confinement in twice the size of the MQW area for fundamental TE mode could be obtained by plotting the obtained values of different QW widths and recess depths, as shown in Figure 3.4 a) and b). For the fundamental TE mode, a deeper recess and a wider QW width results in a higher degree of confinement in the active region and lower losses. The contour lines shown in Figure 3.4 a) and b) represent the number of modes that fulfill the confinement and loss criteria defined in section 3.1.1. Ideally, only a single mode should exist in out structure for the laser to have a narrow linewidth and low noise. It is shown that a larger QW width and deeper recess allow for a larger number of modes to propagate in the structure. An area where only a single mode passes both criteria is obtained by superimposing the two contour plots, as shown by the green area in Figure 3.4 c).

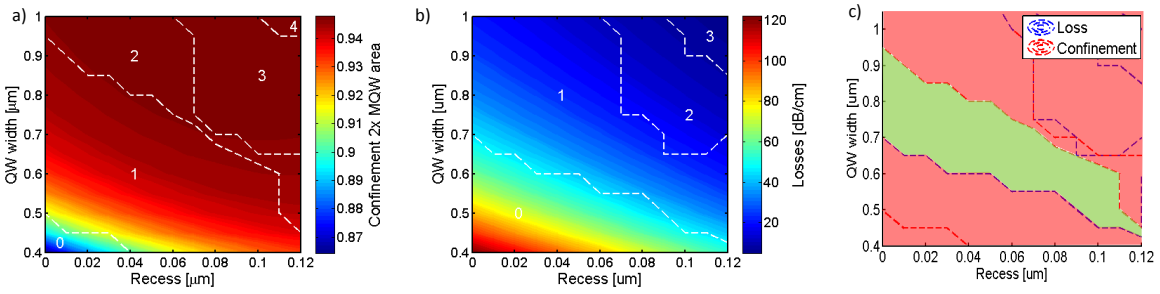

Figure 3.4: Maps of a) the confinement in twice the size of the MQW region and b) the losses generated from simulations where the QW width and the recess depth were varied. The color coded areas represent the values of the fundamental TE mode and the contour lines represent the number of modes fulfilling the confinement and loss criterion respectively. The map a) shows an indication of increased confinement as well as a larger number of modes fulfilling the criterion as the QW width and recess depth increase. The map b). shows an indication of decreased losses as well as a larger number of modes fulfilling the criterion as the QW width and recess depth increase. The map c) shows a superposition of the contour lines from a) and b) indicating an green area for which only a single mode passes both the criteria.

3.1.3 Effect of doping level

To allow carrier-injection into the QWs, the InP contacts need to be doped. A high doping level supplies a large amount of carriers which can be injected into the active material and contribute to the gain. As explained in section 3.1, introducing dopants affects the complex effective refractive index in a material.

An estimation of the total losses for the fundamental TE mode in the InP contacts were simulated by sweeping the doping level for three different quantum well widths of 500, 700 and 1000 nm and a recess of 60nm, as shown in Figure 3.5 a). A drastic increase in losses was seen for doping levels higher than 5E18 cm^{-3}. It is also shown that for the 500 nm QW width, the losses are higher than in the structure with 1000 nm QW width which is an effect of lower confinement factor. In the InP material system, the doping level affects the extinction coefficient for the p-type doping more significantly than for n-type doping, see Appendix C. To find out more precisely how large the difference is, a simulation of variation in n-type and p-type doping level was conducted. For high doping levels, it is clearly shown that the majority of the losses arise from the p-type contact (Figure 3.5 b). Consequently, the doping level should be chosen where the losses are minimized while carrier concentration is still sufficiently high to ensure a low enough series resistance.

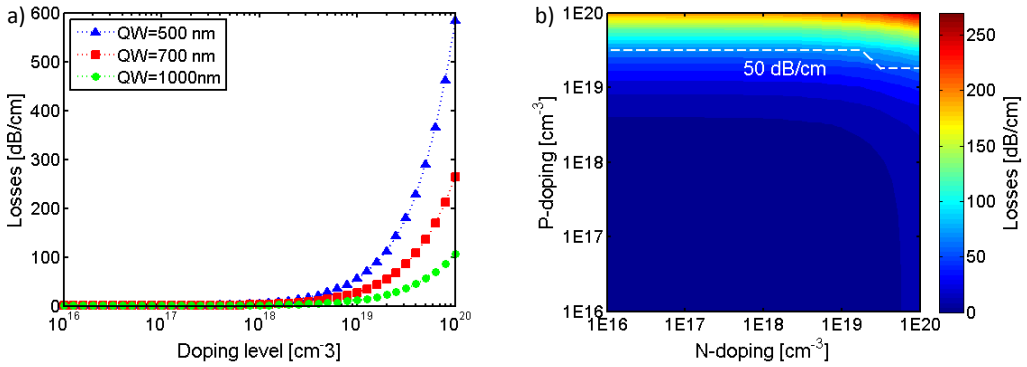

Figure 3.5: a) Simulations of the total losses of the fundamental TE mode in the InP contacts versus doping level for three different quantum well widths of 500, 700 and 1000 nm. b) Simulation of the optical losses of the fundamental TE mode for a variation of n-type and p-type doping levels in a fixed structure with a quantum well with of 700nm and a recess of 60nm.

3.2 Contact resistance versus losses

In section 3.1.2, it was clearly shown that etching a recess in the contacts decreased the amount of modal losses. A simulation of the losses of the fundamental TE mode versus recess depth for three different doping levels of 1E17, 1E18 and 1E19 cm^{-3} was conducted, as shown in Figure 3.6 a). Although a deep recess seems to be favorable, especially for the doping level of 1E19 cm^{-3}, one has to keep in mind that if the recess is larger than 60 nm, which is the depth where the top of the MQW stack is reached, the carrier-injection into the QWs will also be affected. In case the recess is very deep, the cross-section of the contact is reduced and the contact resistance might increase. The resistance can be calculated accordingly:

$$R = \frac{L\rho}{A} = \frac{L}{Anq\mu} \tag{3.1}$$

Where A is the cross-sectional area, L is the length, ρ is the resistivity in the material which is related to the doping level n, the carrier charge q and the carrier mobility μ. The carrier mobility is dependent on the doping level in the material and in our calculations the mobilities for the three different doping levels of 1E17, 1E18 and 1E19 cm^{-3} were determined in different ways for the n- and p-doped InP contacts. The mobilities for the n-doped InP contact was extrapolated from Hall measurements performed on six epitaxially grown InP samples of different doping levels while the mobilities for the p-doped InP contact was estimated based on reported literature values [27–29].

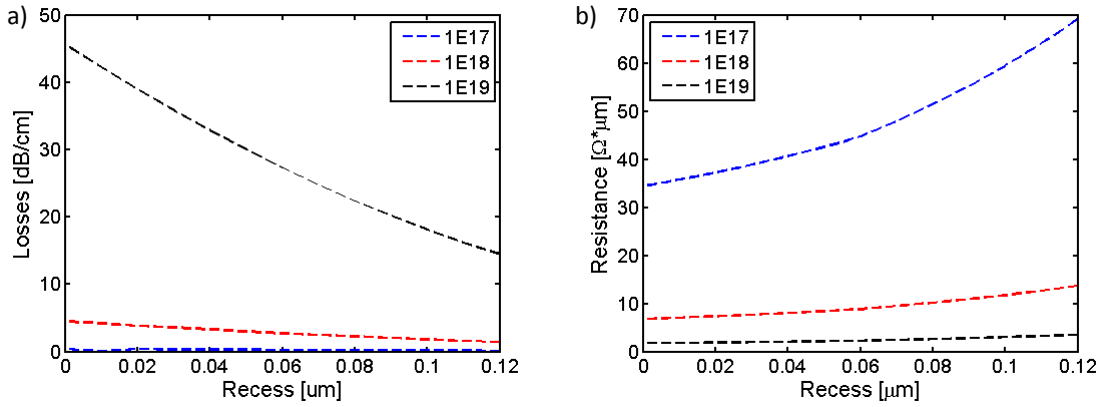

Figure 3.6: a) Simulation of the losses for the fundamental TE mode versus the recess depth for three different doping levels of 1E17, 1E18 and 1E19 cm^{-3}, indicating an reduction in losses for larger recesses. b) Estimation of the contact resistance versus the recess depth indicating an increased resistance for low doping levels as the recess depth is increased.

A model was constructed in Microsoft Excel to give a rough estimation of how the recess depth affects the resistance in the contacts. Figure 3.7 shows a schematic illustration of the model based on four series resistances. If the recess is less than 60nm, the current can flow straight into the MQW region and R2 and R4 are equal to zero. The percentages indicated in Figure 3.7 represent the contribution of each series resistance for the case of a recess of 120 nm and a doping level of 1E19 cm^{-3}. It is clear that the main resistance contribution originates for the p-doped contact where the width of the contact is the key parameter to consider when designing the contact dimensions. Figure 3.6 b) shows the resistance for three different doping levels of 1E17, 1E18 and 1E19 cm^{-3} versus the recess depth. For low doping levels, an increase in recess depth results in a larger resistance. In the active structures, a recess depth should be used where there is an optimum balance between losses and contact resistance.

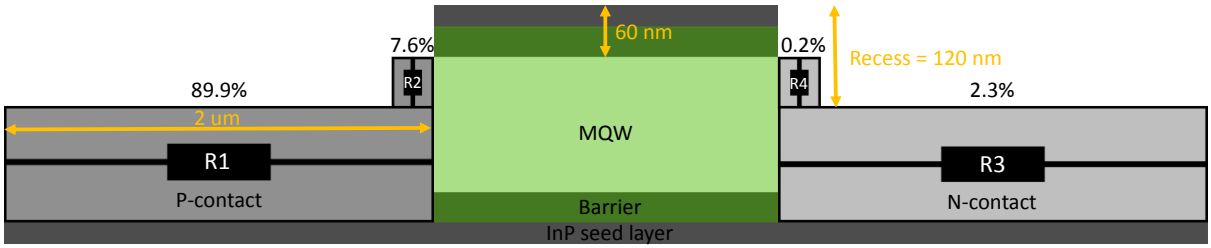

Figure 3.7: Schematic illustration of our resistance model based on four series resistances. The percentages indicate the contribution of each resistance to the total resistance for a recess of 120 nm and a doping level of 1E19 cm^{-3}. It is clearly shown that the main contribution to the total resistance originates from the p-contact.

3.3 Laser performance estimation

The performance of a laser, in terms of threshold current and optical power output, can be estimated by solving the rate equations explained in section 2.2.2. It is expected that an increase in cavity length should increase the threshold current and that the optical power output increases when a larger bias is applied.

A theoretical model of our laser design was constructed in Matlab, using the following parameter values taken from literature; $\eta_i = 80\%$, $B = 1.5^{-10}$ cm^3s^{-1}, $N_{tr} = 2.24^{18}$ cm^{-3}, $g_0 = 2500$ cm^{-1}, $\alpha_i = 30$ dB/cm and $R = 0.9$. The affect of thermal heating and Auger electron recombination on the lasing threshold and the optical output power were not taken into consideration. Unlike the optical simulations where the QWs and barriers were assumed to be a single region, this model considered the confinement factor inside

a single quantum well. Because approximately one third of the active region consisted of the QWs (the rest is barrier material), a single confinement factor of a few percent is expected. Figure 3.8 a) shows the threshold current versus the cavity length for two different single QW confinement factors (Γ) of 3% and 6% . As expected, the lasing threshold increases with cavity length and is higher for the lower confinement factor (3%). A few mW in output power can be obtained for a laser with a 700 nm wide and 350 µm long cavity and a layer stack containing seven QWs with a single confinement factor of 6%, if a driving current larger than 8mA is applied, as shown in Figure 3.8 b).

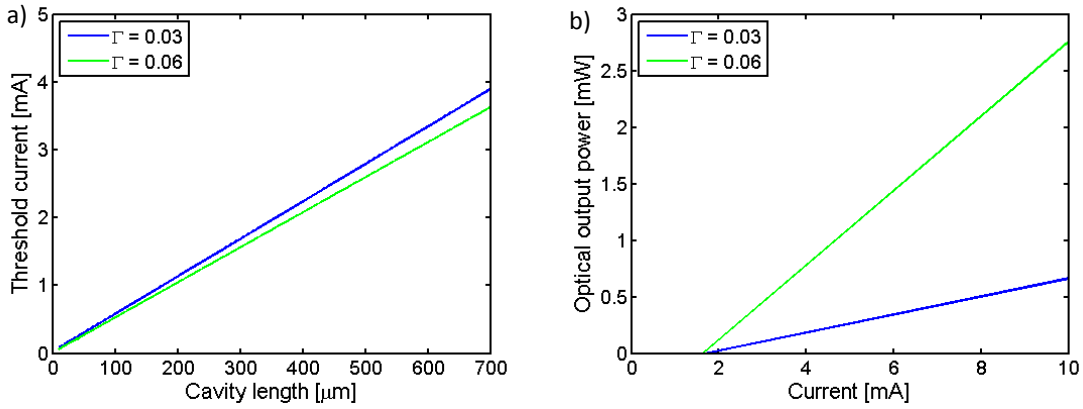

Figure 3.8: Simulation results for two different single QW confinement factors of 3% and 6% showing a) the threshold current versus cavity and b) the optical output power versus applied bias for a 700 nm wide and 350 µm long cavity with a MQW stack containing seven QWs.

3.4 Summary of device design

The optical simulations resulted in a range of suitable laser dimensions supporting only a single mode according to the defined criteria. The estimation of the contact resistance revealed that the majority of the resistance originates from the p-contact and that the width of the contact has a larger impact on the total resistance than the depth of the recess. However, it is not completely understood how the recess depth affects the carrier injection into the quantum wells which was the reason for choosing the recess depth to be 60 nm. For a 60nm recess, quantum well widths around 700 nm should support only a single mode accodring to Figure 3.4 c). Consequently, the mask design of the active lasers contained an array of devices with quantum well widths varied around 700 nm. The doping level of both the n- and p-doped InP contacts were chosen to be 1E19 cm^{-3} which was assumed to be high enough to provide a sufficient amount of carriers without contributing to a significant increase of absorption losses.

Chapter 4

Active devices

4.1 General process concept

As explained in the introduction, fabrication of a lateral current injection laser is a rather complex process containing many steps. To avoid time consuming mistakes on the complete device structures, some of the critical steps have been first developed on test pieces before fabrication of the real lasers. A sequence of the key fabrication steps is schematically illustrated in Figure 4.1 (a-i) and more details will be given in the following sections 4.2 - 4.6.

The fabrication process started with the epitaxial growth of the active III-V materials i.e. the multiquantum well stack (MQW) by metalorganic chemical vapor deposition (MOCVD). Next, the MQW stack was integrated on a silicon dioxide (SiO_2) layer on a silicon substrate through direct wafer bonding, as shown in Figure 4.1 a). Alignment marks of tungsten were fabricated to aid the alignment procedure in future lithography processes. Afterwards, a silicon nitride (SiN) hard mask was deposited on the MQW stack by plasma-enhanced chemical vapor deposition (PECVD). It was used as a mask for patterning of the active region and to prevent growth on top of the MQW stack. The dimensions chosen from the results of the optical simulations in section 3.1.2 were patterned on top of the SiN by electron-beam lithography (EBL). Once the MQW pattern was developed, the SiN hard mask was etched down by reactive ion etching (RIE) and the MQW region was defined by wet etching of the III-V materials, as shown in Figure 4.1 b) and c). The III-V wet etch was isotropic, meaning that it occurred in both the vertical and horizontal directions and produced an undercut below the SiN. To allow the current injection into the MQW region, *in situ* doped n- and p-type InP contacts were regrown by MOCVD. Because the regrowth was performed in two steps, a masked selective area epitaxy process was adopted. A tetraethyl orthosilicate (TEOS) mask was deposited by

PECVD and the areas where no growth should occur, i.e. the area for the p-type contact, was patterned by EBL. To open up the TEOS in the areas selected for n-type growth, a combination of dry and wet etching was performed, as shown in Figure 4.1 d). After the n-type regrowth shown in Figure 4.1 e), the same procedure was conducted for the p-type InP contact. Following the regrowth procedures, Bragg reflectors, access waveguides and grating couplers were formed in the regrown n-type InP material by inductively couple plasma (ICP) so that it would be possible to characterize the light created in the optical cavity. As a final step, a protective TEOS cladding was deposited by PECVD and metal contacts were fabricated to allow biasing of the devices, as shown in Figure 4.1 h) and i).

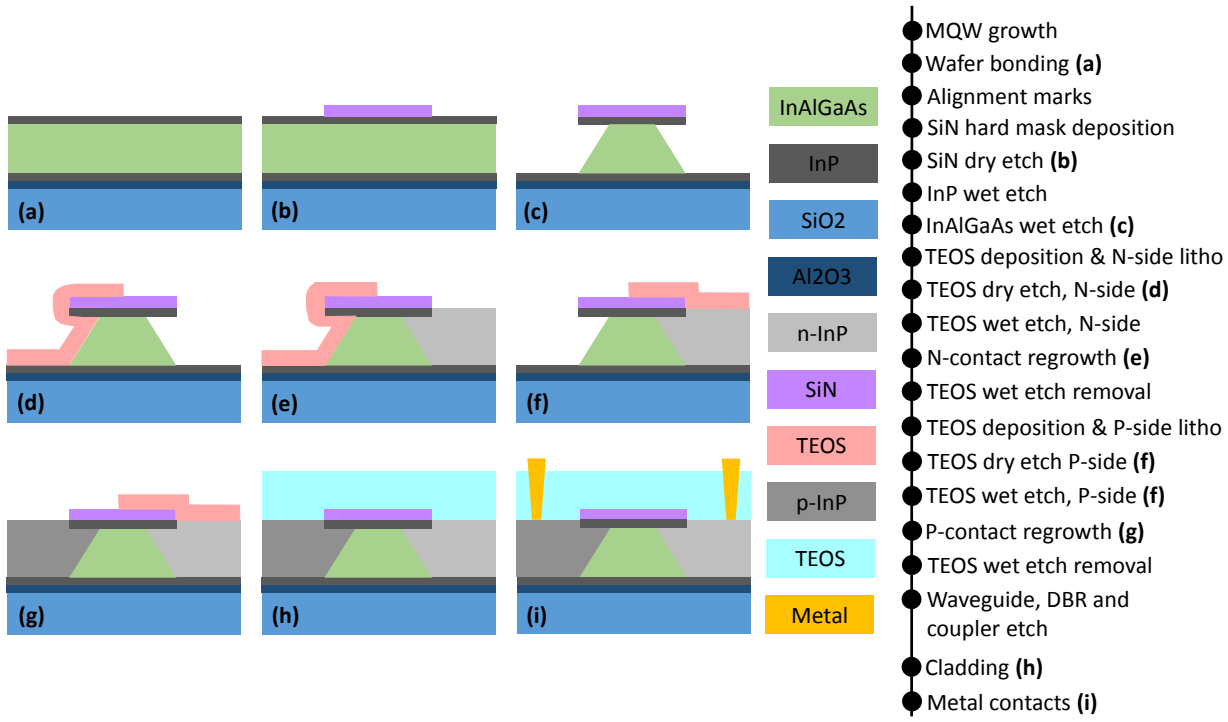

Figure 4.1: The legend to the right describes constituent steps in the fabrication process and schematic images illustrates nine of the main fabrication steps. a) Shows the MQW stack bonded to the silicon oxide layer of a silicon substrate followed by b) a SiN hard mask deposited and patterned according to the dimensions chosen from the simulation results in section 3.1.2. c) Illustrates the wet etching of the active material and d) the deposition and patterning of a TEOS mask opened up for selective n-type contact regrowth. e) Shows the structure after n-type contact regrowth and f) the deposition and patterning of a TEOS mask opened up for p-type contact regrowth. g) Illustrates the structure after p-type contact regrowth. h) Shows the structure after deposition of a protective TEOS cladding and finally i) illustrates the structure after metal contact fabrication.

4.2 Epitaxial growth of the multiquantum well stack

The multiquantum well stack, acting as active material in the laser, had a rather complicated design to meet the processing and performance requirements. First, IBM's silicon photonics platform was designed to operate at a wavelength of 1300 nm. Consequently, the multiquantum well stack had to be grown so that it emits light at the right wavelength. From experience within the research group at IBM, the emission peak is expected to be red-shifted by about 20 nm during operation due to heating, which was why the target wavelength was instead set to 1280 nm. Secondly, for the laser to be used as a component in a silicon photonic chip, the MQW stack had to be able to be integrated on a SiO_2 substrate. These requirements lead to the proposed stack illustrated in Figure 4.2. The epitaxial stack was grown by metalorganic chemical vapor deposition (MOCVD) in a system from Veeco.

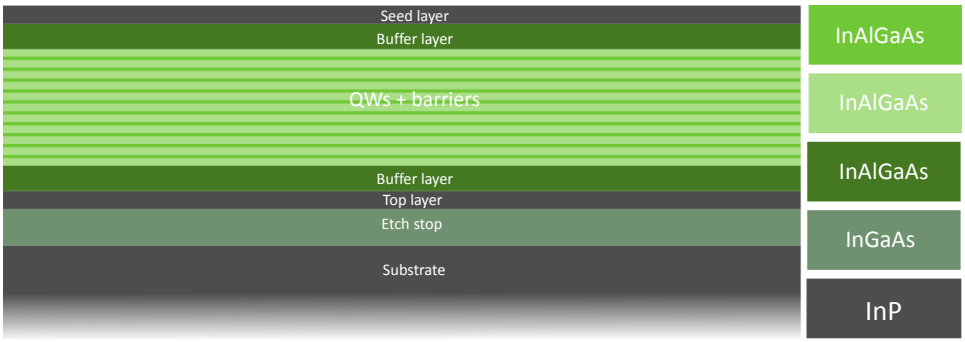

Figure 4.2: Schematic of the epitaxial MQW stack consisting of 10 QWs separated by 11 barrier layers forming the active region. The active region is sandwiched between two buffer and two InP layers. The epitaxial stack is grown on an InP substrate with an etch stop layer incoporated.

Starting from the bottom of the epitaxial stack, an undoped InP wafer was used as growth substrate. The first 50nm thick InGaAs layer seen in Figure 4.2, was an etch-stop layer required for the removal of the InP donor wafer during the wafer bonding. The bonding process is described in more detail in the following section (section 4.3). The 25nm InP layer was used for passivation and to make the structure symmetric. The 35nm $In_{0.53}Al_{0.30}Ga_{0.17}As$ layer served as a buffer layer increasing the optical mode confinement and preventing carrier leakage. The alternating striped light green area comprises 10 quantum wells separated by 11 barrier layers. The quantum wells consist of an approximately 5 nm thick $In_{0.62}Al_{0.29}Ga_{0.22}As$ layers and the barriers of 10nm thick $In_{0.49}Al_{0.14}Ga_{0.24}As$ layers. Similar to the layers below the active material, a 35nm thick $In_{0.53}Al_{0.30}Ga_{0.17}As$ buffer layer and a 25 nm thick InP layer were grown on top. The InP

layer acted as a seed layer for the regrowth later on in the process.

Our previously performed photoluminescence (PL) measurement revealed that our original structure had an emission peak at a wavelength of 1307 nm which was approximately 30 nm off from the targeted 1280 nm. To decrease the wavelength of emitted photons their energy needed to be increased. Thus, an increase in the bandgap size was needed. This was achieved by decreasing the quantum wells thicknesses from 5.5 to 5 nm resulting in a blue-shift with an emission peak at 1288 nm, as shown in Figure 4.3

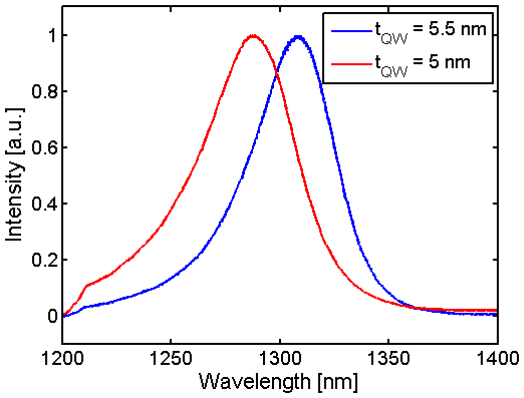

Figure 4.3: Photoluminescence spectrum of two epitaxial multiquantum well stacks. The blue sample has a quantum well thickness of 5.5 nm and the red sample has a quantum well thickness of 5.0 nm.

4.3 Wafer bonding

In order to integrate the MQW laser stack on a silicon dioxide layer of an oxidized silicon wafer, a direct wafer bonding process was performed [30]. In this method, a 15 nm thick Al_2O_3 layer was deposited by atomic layer deposition (ALD) on both the target (SiO_2) and donor (III-V) wafers. By flipping the III-V wafer upside down, bonding of the two wafers could be obtained by pressing the oxidized surfaces together under thermal treatment at 300°C for 2 hrs. Once the bonding was complete, the InP donor wafer was removed by chemical wet etching in hydrochloric acid (HCl) that lasted until the InGaAs etch stop layer was reached. The above mentioned process steps are schematically illustrated in Figure 4.4.

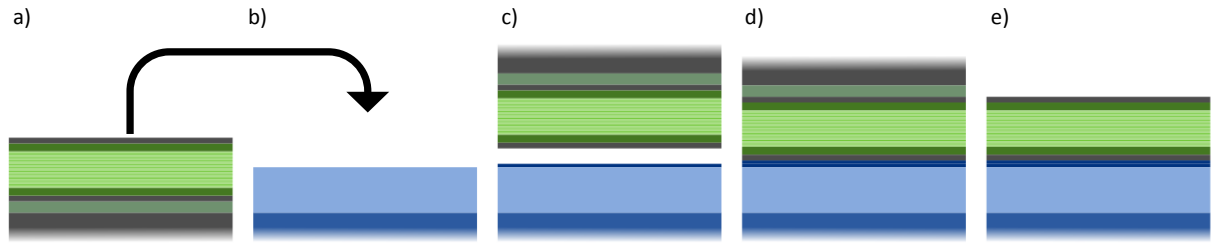

Figure 4.4: Schematic illustrations of a) epitaxially grown multiquantum well structure on InP (donor) wafer, b) SiO_2 (target) wafer, c) Al_2O_3 deposition flollowed by flipping, d) wafer bonding under annealing at 300°C for 2 hrs and e) InP donor wafer removal by HCl wet etching resulting in the desired structure.

4.4 Regrowth masking

Before patterning and etching the structures chosen from the optical simulations, a 50 nm thick silicon nitride (SiN) hard mask was deposited on the top InP layer by PECVD. The purpose of the SiN mask was to prevent growth on the top InP layer during the selective area regrowths of the n-and p-doped InP contacts and for patterning of the active region. As mentioned in Section 4.1, TEOS was used for masking the area where no growth should take place. Prior to depositing TEOS on the real wafers, the process was developed on test-pieces. First, 50nm TEOS was deposited and patterned by EBL. A cross-sectional scanning electron microscopy (SEM) image of such fabricated structure is shown in Figure 4.5 a) where the TEOS layer is highlighted in green. The TEOS mask was not completely uniform and did not have the same thickness on all areas, in particular in the undercut region as it is not directly exposed to the ion bombardment from the plasma. Still, it could cover the undercut area. Next, the areas where growth should occur were opened by RIE (Figure 4.5 b). As some TEOS remained in the undercut, the sample was etched for 3min in DHF-1% resulting in complete removal of the TEOS (Figure 4.5 c).

During the regrowth process, a total of four TEOS wet etch cycles had to be conducted. To make sure that a sufficient amount of SiN remained after the etching, the etch rate of TEOS had to be at least 4 times the SiN etch rate, given that the thicknesses of the SiN and TEOS layers were the same. Thus, a 1:8 selectivity between SiN and TEOS was targeted to compensate for possible process inaccuracies such as too thick TEOS layers and prolonged etch times but most importantly to ensure that enough SiN remained at the end of the four etch cycles.

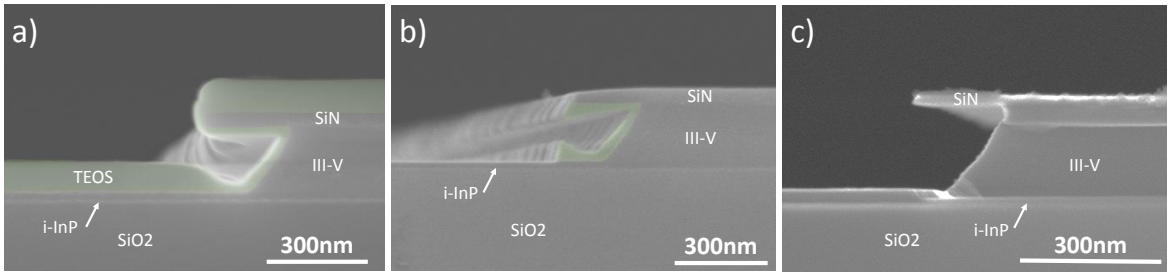

Figure 4.5: Cross-sectional SEM images of a fabricated sample where the green shaded areas show the TEOS layer. a) After deposition of TEOS. b) After RIE process and removal of TEOS on the desired areas for growth. c) After 3 min DHF-1% wet-etching to assure complete removal of TEOS in the undercut.

The chemical solution used to etch the TEOS was hydrofluoric acid diluted in deionized water with a concentration of 1% (DHF-1%). By means of ellipsometry measurements of the TEOS layer on a test-piece, the thicknesses of the layer before and after the wet etch were determined. From the ellipsometry thickness results, the TEOS etch rate was determined to 17.5 nm/min.

In order to obtain a selectivity of 1:8 between SiN and TEOS, the etch rate of SiN in DHF-1% can be altered by changing the composition of the SiN_x. Silicon nitrides with low Si content has a fast etch rate that can be decreased by increasing the amount of Si. However, too much Si could form tiny particles inside the SiN layer. By varying the silane (SiH_4) flow in the PECVD reactor, SiN layers with different compositions were obtained. The same procedure for determining the TEOS etch rate in DHF-1% was conducted also on the different silicon nitrides. Table 4.1 shows the result of SiN etch rate and SiN:TEOS selectivity for samples grown by various silane (SiH_4) flows.

SiH_4 flow [sccm]	**Etch-rate in DHF-1% [nm/min]**	**Selectivity SiN:TEOS**
187	5.10	1:3.4
200	4.43	1:4.0
250	2.67	1:6.4
275	2.33	1:7.4

Table 4.1: SiN etch rates (nm/min) in DHF-1% measured for samples grown with various silane flows as well as the resulting selectivity between SiN and TEOS.

Once the development of the TEOS masking/unmasking process and SiN tuning were finished, the real wafers were processed. Prior to the SiN deposition the wafer was cleaned

in HF:ethanol (1:100 ratio) for 1 min followed by 1 min rinse in DI water and then directly transferred into the PECVD tool. The SiN hard mask with a selectivity of 1:7.4 to TEOS was deposited followed by spin-coating an approximately 150 nm thick resist on the wafer. The pattern of the active material structures was defined by EBL. The SiN hard mask was etch by RIE in CHF_3:O_2 for 1 min and 50 sec.

4.5 Active material etching

Etching the MQW stack to create the active material waveguide was one of the most critical steps in the fabrication process. It was essential to avoid having any contaminating residuals on the side walls because they could contribute to the carrier recombination and imped the carrier injection into the active region. Additionally, the presence of residuals on the side walls could potentially hamper the crystalline merging of the InP contacts with the MQW stack during regrowth. Both inductively coupled plasma (ICP) dry etching and chemical wet etching could be used to etch the active material. Even though ICP etching has the possibility to perfectly etch vertical side walls, it is known to leave residual materials, an effect that was crucial to avoid in our process. To ensure the cleanliness of the side walls, a wet etch process was chosen. The wet etch had to be conducted in two steps because it was essential to keep the bottom InP seed layer after etching of the InAlGaAs layers. Therefore, a selective etchant that would only etch the InAlGaAs layer but not the InP layer was required.

Prior to the fabrication of the active structures, we investigated the etch rate of InP in diluted HCl (37%) on test-pieces. A photoresist was deposited and patterned on a blanket InP wafer. The sample was etched for 1 min and the step height before and after the etching was measured with a profilometer. The etch rate was then determined from the step height and etching time for various HCl:H_2O dilutions, as shown in Figure 4.6 a). As an example, a diluted HCl:H_2O solution with a ratio of 3:4 etched 25nm of InP in 30 sec. Secondly, the vertical and lateral etch depth of InAlGaAs in H_3PO_4:H_2O_2:H_2O solution with the ratios 4:3:100, was investigated as a function of time (20-120 sec). The vertical and lateral etch depths of such samples were measured by cross-sectional SEM images (Figure 4.7). From Figure 4.6 b) it was possible to extrapolate the vertical InAlGaAs etch rate to approximately 120 nm/min. Both the lateral and vertical etch rates are similar indicating that the etch rate has little dependence on the crystalline orientation.

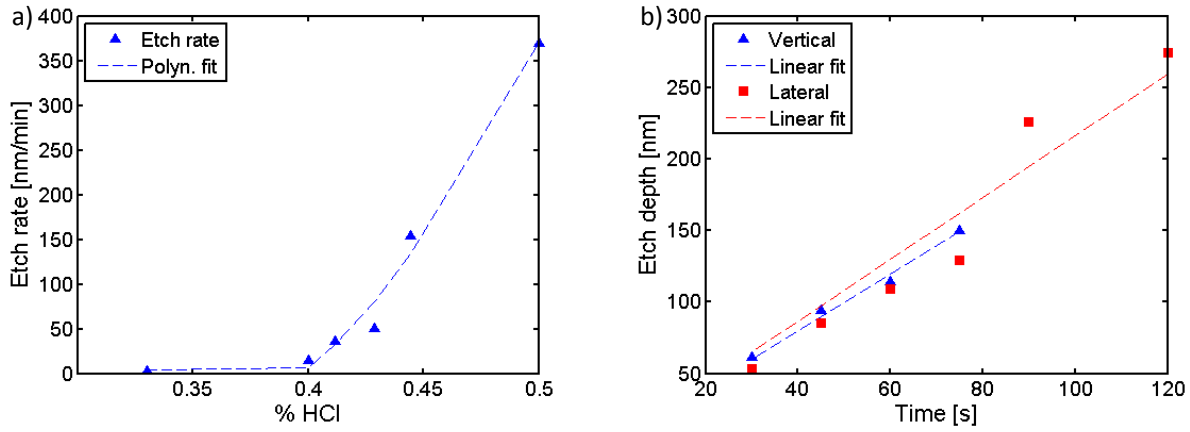

Figure 4.6: a) Etch rate of InP with respect to various HCl concentrations (dilution ratios), obtained by measuring the step heights of the sample before and after etching by a profilometer. b) Vertical and lateral etch depth of InAlGaAs etched in H_3PO_4:H_2O_2:H_2O solution (ratios 4:3:100) as a function of time, suggesting a vertical etch rate of 120 nm/min.

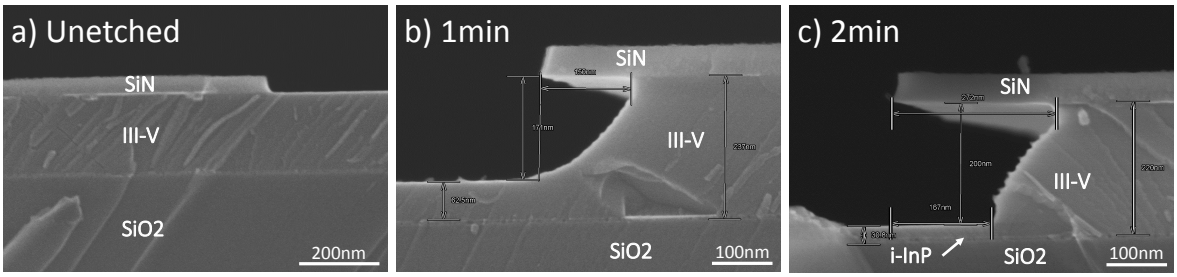

Figure 4.7: Cross-sectional SEM images of an InAlGaAs layer. a) Before etching, b) after 1 min, c) after 2 min etching in H_3PO_4:H_2O_2:H_2O solution.

After the initial investigation on the etching rates, the real wafer was etched in a diluted HCl:H_2O solution (3:4 ratio) for 3.5 minutes followed by another wet etching in the H_3PO_4:H_2O_2:H_2O solution (4:3:100 ratio) for approximately 2 min.

4.6 Epitaxial contact regrowth

Epitaxial regrowth of the n- and p-doped InP contacts were conducted in two separate steps. Similar to the active material etching, this process was also very critical because several requirements needed to be fulfilled. As explained in Section 4.4, masking and opening the selected areas of the wafer was necessary to separate the n- and p-doped areas. Furthermore, the regrown contacts had to be uniform and of 255 nm thickness, with the possibility to control the *in situ* doping level. In addition, the contact material

had to merge laterally with the active material to allow carrier injection into the MQW stack. In case the regrowth would be non-uniform along the cavity, the effective refractive index and mode profile would vary along the cavity, causing an increase of the losses.

Based on the investigation of the doping level (described in section 3.5), a doping level of 1E19 cm^{-3} was chosen for both contacts. Prior to conducting the regrowth on the real wafers, a calibration run of the n-type doping level was performed. Multiple samples of 200 nm Sn-doped InP layers were grown on InP substrates. It was concluded that a flow of 35 sccm for the Sn precursor (TESn) resulted in a doping level of 1.34E19 cm^{-3}. The doping levels were determined by performing Hall measurements, the technique is described in more detail in Appendix B.

4.6.1 Investigation of surface preparation

The surface preparation idea (prior to the regrowth) was to first clean the side walls from residual particles and oxides that may had formed during storage by applying the InAlGaAs wet etch solution developed in section 4.5. This step was followed by a surface passivation by dipping the sample into diluted sulfuric acid, H_2SO_4:H_2O (1:2 ratio). The principle is that a sulfur passivation would form on the side walls and ensure that no native oxide could regrow between the cleaning and prior to the growth. It should be noted that, unlike the case of In native oxide, Al oxides are very stable and difficult to thermally desorb in the epitaxy reactor chamber and their presence should be avoided if possible. After the dip and before the sample was loaded into the MOCVD system, it was rinsed in DI water to remove any excess material (such as H_2SO_4) left on the sample's surface. After loading the sample into the MOCVD system, the temperature was raised, leading sulfur to desorption and hence providing a clean surface for the growth. The outcome of the regrowth was found to largely depend on the surface condition of such samples.

The regrowth tests were performed on several test samples before fabricating the real wafer. The preparation of the test samples also included patterning with wider SiN hard masks than the real samples. After the patterning, the MQW stack was wet etch down to form the MQW waveguides, no TEOS masking was performed. All samples were first etched for approximately 10 sec in H_3PO_4:H_2O_2:H_2O solution (4:3:100 ratio). The sulfur passivation and rinsing time were varied between the samples, details can be seen in the list below.

Sample A - 5 min H_2SO_4:H_2O, 1 min rinse in DI water.

Sample B - 1 min H_2SO_4:H_2O, 1 min rinse in DI water.

Sample C - 1 min H_2SO_4:H_2O, 1 min rinse in DI water, approx. 2 hrs air storage.

Sample D - 1 min H_2SO_4:H_2O, 10 min rinse in DI water.

It should be noted that all four samples were grown with the same growth conditions and their surface morphology was characterized by SEM. If the undercut below the SiN hard mask, which was created from the wet etching process, was filled up with material it indicated that the n-InP material had merged with the side walls of the MQW stack. In the top view SEM images of such a case, only the SiN hard mask can be distinguished. However, if the undercut was not filled with material (indicating n-InP material did not merge with the MQW side walls), a dark line appeared at the edge of the SiN hard mask. The SEM results of the test-runs (Figure 4.8) showed that the regrowth was extremely sensitive to the surface preparation method. From Figure 4.8 a) and b) it can be seen that the short rinsing time of sample A and B, led to formation of large holes in the regrown n-InP material. A longer sulfur passivation time showed no indication of improved merging. In sample C and D, for which the storage and rinsing times had been increased, the merging was improved and the regrown n-InP material formed without any holes. For the time being, the surface preparation methods for sample C and D were regarded to be sufficient enough for the process of the active devices to be resumed. In the future, if the focus is rather to optimize the laser performance than simply demonstrating a lasing device, the surface preparation should be futher investigated.

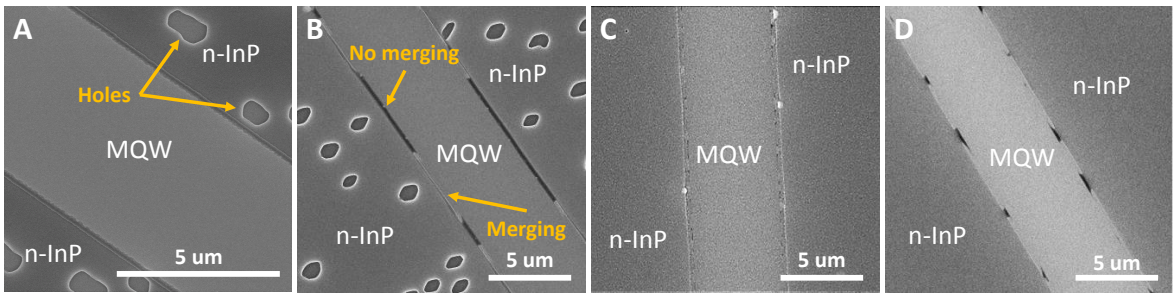

Figure 4.8: Top view SEM images of four samples prepared with different sulfur passivation, rinsing and storage times. Sample A and B had been prepared with a short rinsing time which resulted in formation of holes in the regrown n-InP material and poor merging. Sample C and D had been stored in air for approx. 2 hrs and rinsed for 10 min respectively and showed improved merging without holes in the regrown n-InP material.

4.6.2 Transmission electron microscopy analysis

Although the merging seemed to be sufficient for sample C and D, transmission electron microscopy (TEM) images were taken across a MQW waveguide to provide a better understanding of the merging process, as shown in Figure 4.9. The regrowth was initiated by growing a thin InGaAs layer before changing to n-InP growth. During the n-InP growth, thin layers of InGaAs markers were grown after every 50 nm n-InP to create a contrast difference in the image. By introducing markers, we were able to study how the growth progressed. From the overview image (Figure 4.9 a), it can be seen that the merging with the side wall was not uniform but occurred suddenly during the fourth cycle of InP. The darker grey area seen on the side wall is an accumulation of InGaAs. Figure 4.9 b) shows an HRTEM of the MQW side wall (indicated by the green box in Figure 4.9 a). The material is crystalline and not many defects can be seen. Therefore, there should not be any problems to inject carriers into the quantum wells.

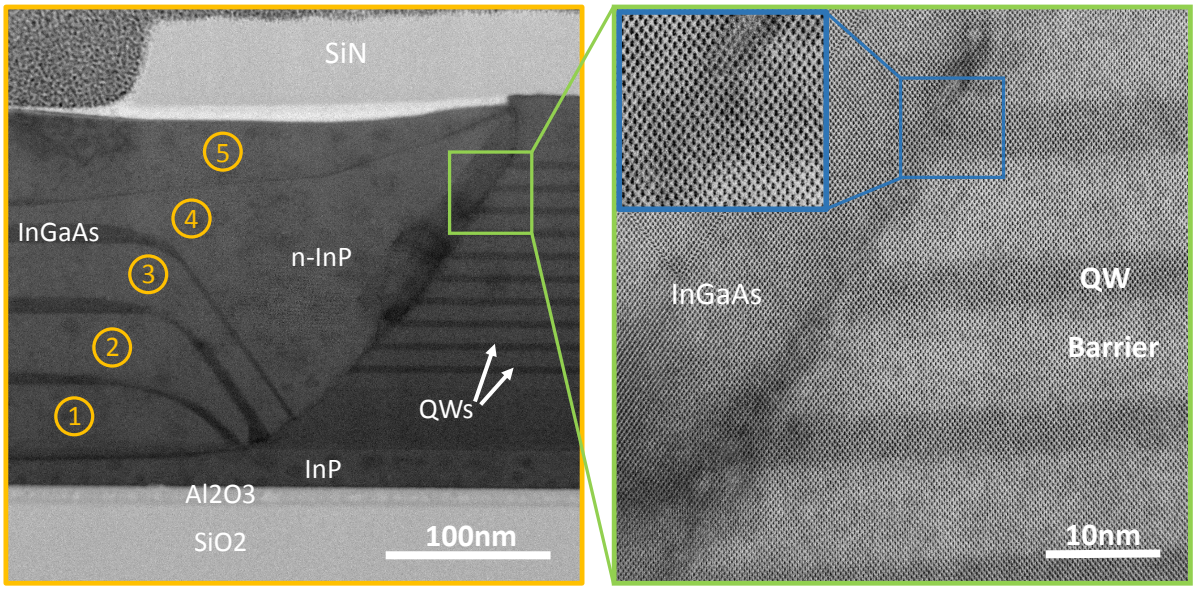

Figure 4.9: Cross-sectional TEM images of a sample where the n-InP contact had merged with the sidewall of the MQW stack. The HRTEM image (green box) indicates a crystalline material without many defects.

Ideally, the InP material should have a uniform lateral growth rate and merge with the MQW side wall as the growth proceeds. In our sample a difference in the vertical and the lateral growth rates can be noticed when studying how the InP thickness varies between two InGaAs layers when moving from left to right (Figure 4.9). In the lower right corner where the InAlGaAs stack starts, it is clearly seen that the lateral growth

is impeded and "rotates" around this point indicating that the InAlGaAs surface was not clean enough. Energy dispersive x-ray spectroscopy (EDS) is a technique used for elemental analysis and could potentially give us information about whether the surface was contaminated by for example an Al-oxide layer. The technique is based on focusing a beam of high-energy electrons on a specific area of the sample. Through interactions between the beam electrons and the atoms in the area, x-rays that are characteristic to the elements present in the specific area are emitted. By scanning the electron beam over a larger region it is possible to obtain elemental maps [31]. Figure 4.10 a) shows an overview TEM image of a sample where the contact had merged with the MQW side wall. An HRTEM image over the area where the lateral growth was impeded (indicated by the yellow box in Figure 4.10 a) is shown in Figure 4.10 b). Figure 4.10 c) and d) shows two high resolution EDS maps acquired by scanning transmission electron microscopy (STEM) where the colors correspond to the presence of different elements. The presence of aluminum in the MQW area can be clearly seen as the pink area in c). Figure 4.10 d) shows that there is a high amount of oxygen (blue color) present at the interface between the MQW side wall and the regrown material. As anticipated, there was an Al-oxide region present which might have impeded the lateral merging.

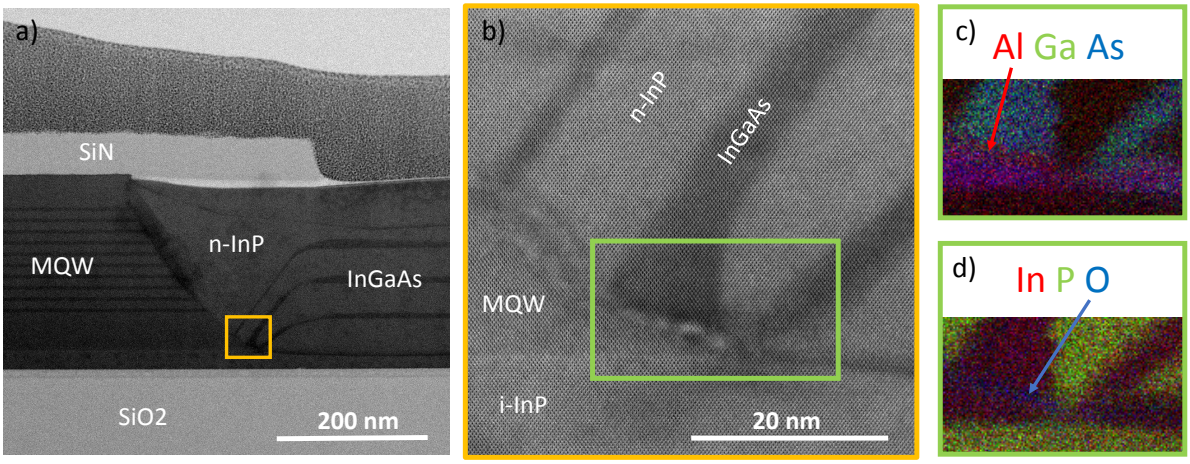

Figure 4.10: a) Shows a cross-sectional TEM image of a sample where the InP material had merged with the MQW side wall and b) shows a magnification of the area in the corner where the merging was impeded. EDS maps obtained by STEM showing the elemental presence of c) aluminum (red), gallium (green), arsenic (blue) and d) indium (red), phosphorus (green) and oxygen (blue).

4.6.3 Active samples

The surface preparation for sample D (described in section 4.6.1) was found satisfactory and the method was chosen for processing of the real devices. The regrowth of the n-contact started by depositing a 3 nm Al_2O_3 layer by atomic layer deposition (ALD) to promote the following 50 nm thick deposition of TEOS by PECVD. A positive e-beam resist was spin-coated on top of the TEOS and patterned so that the areas where no n-type InP should be grown were covered, as shown in Figure 4.11 a). The TEOS in the n-type area was then removed by RIE and 90 sec dip in DHF-1%. The resist was stripped and the sample was cleaned for 10 sec in H_3PO_4:H_2O_2:H_2O solution followed by a 1 min H_2SO_4:H_2O passivation and rinsing in DI water for 10 min. After the cleaning and passivation steps, the sample was loaded directly into the MOCVD and the n-doped InP contact was regrown. The result was unfortunately unsuccessful in several aspects, as shown in Figure 4.11 b). The TEOS masking was insufficient leading to growth on the p-side. The reason for growth on the p-side could be that the chemicals used during the surface preparation procedure removed TEOS in the undercut also on the p-side, due to non-uniform thickness or quality. This would leave both sides of the waveguide open for growth. Additionally, the merging on the n-side was not satisfactory and the n-InP layer thickness was significantly too large.

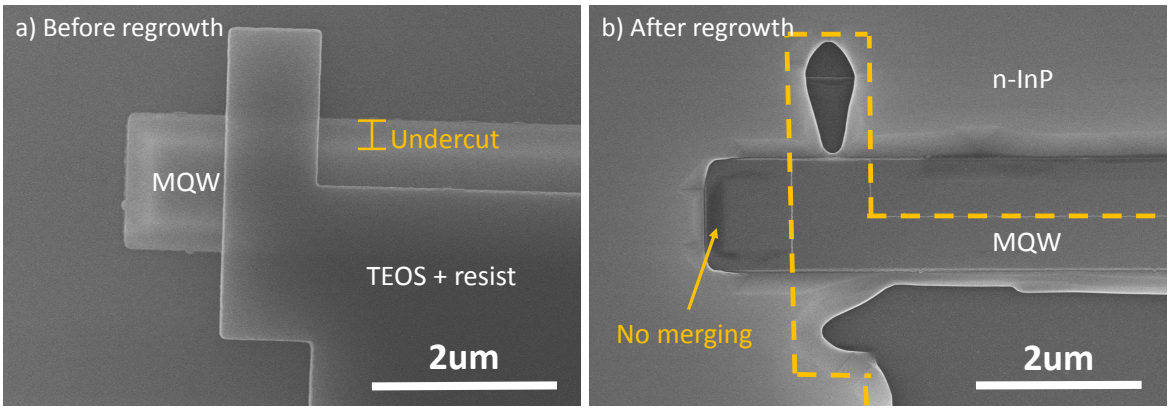

Figure 4.11: Top view SEM images of a MQW waveguide a) before and b) after n-type contact regrowth.

An investigation of what steps in the process where the error originated from was conducted. A new sample was processed where every step of the regrowth masking process was characterized by SEM, see Figure 4.12. After the TEOS dry etch, image a), the sample looked good but after the DHF-1% dip, image b), one could see that TEOS had been removed underneath the resist. The image also shows that the TEOS in the undercut had been cleaned but left residual material around the waveguide. Image c)

shows a narrow waveguide after the resist strip. As the results show, the SiN hard mask had been removed during the resist strip. We can also see that the DHF-1% dip had etched a larger amount of TEOS near the top of the waveguide than near the bottom. This effect was reinforced after 10 sec H_3PO_4:H_2O_2:H_2O dip, image d). Clearly, the quality of the TEOS decreases further up in the undercut which is a consequence of having a PECVD process. In the undercut region, the area is less exposed to the ion bombardment from the plasma, hence a lower film density with more impurities. The lower material quality largely affects the wet etching behavior of TEOS.

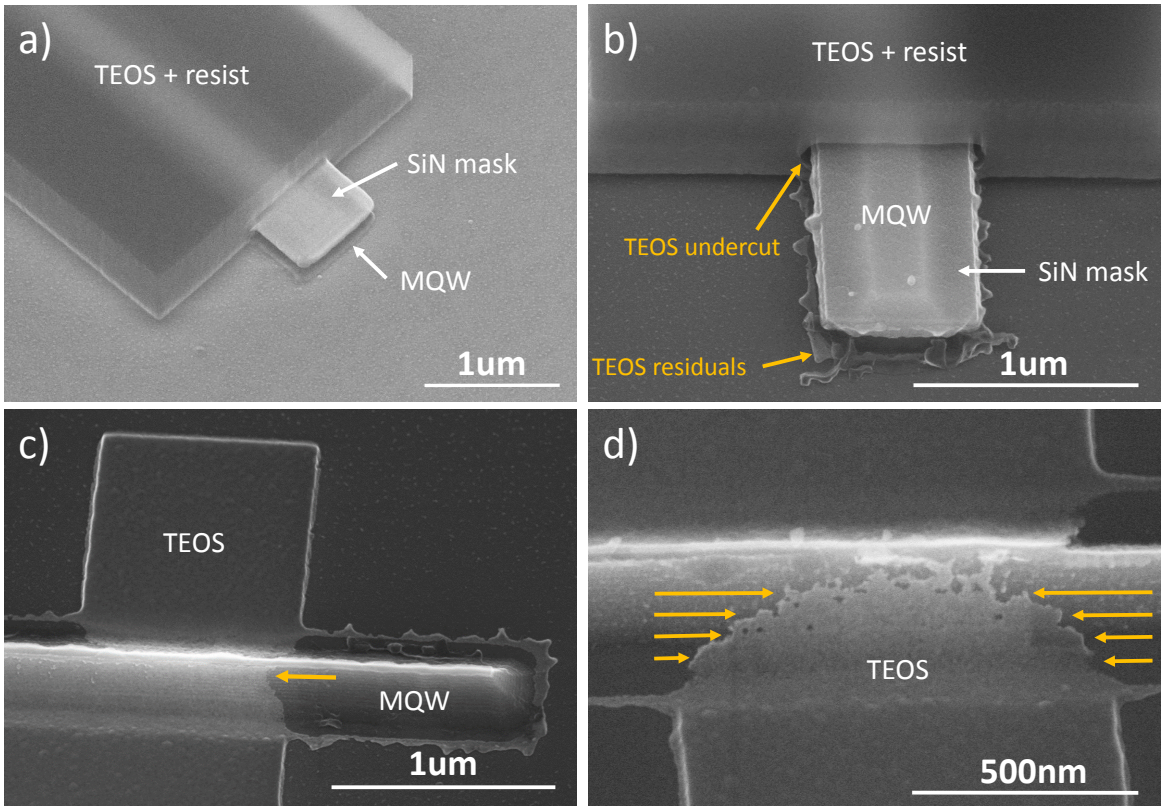

Figure 4.12: Tilted view SEM images of surface preparation procedure. a) After EBL and TEOS dry etching. b) After 1 min DHF-1% etch for removal of TEOS in undercut. c) After e-beam resist strip, image shows MQW waveguide where the SiN hard mask had come off during the strip. d) After 10 sec H_3PO_4:H_2O_2:H_2O wet etch.

Based on the investigation above, it was decided that the H_3PO_4:H_2O_2:H_2O cleaning step should be skipped and instead, a 1 min dipping in HCl:H_2O (1:5 ratio) solution followed by 2 min rinse in DI should be used for the passivation. Corrections were made in the MOCVD recipe to adjust for the InP contact thickness. The TEOS mask layer was made larger to allow for more overetching during the processes. The result of the regrowth plus the second layer of TEOS (prepared for the p-type regrowth) can be

seen in Figure 4.13. The merging on the n-side and the masking on the p-side are still unsatisfactory. Figure 4.13 b) shows a cross-sectional dark field (DF) TEM image of the n-side where it is evident that the n-InP did not merge with the MQW side wall, only a small area in the corner of the undercut was filled up with n-InP material. A thin black line can be seen along the MQW side walls which could potentially be residues from the TEOS mask or an Al-oxide. Additionally, the second TEOS mask does not cover all areas in the undercut. As an example, the "ceiling" of the i-InP in the undercut is left completely bare. It is observed in Figure 4.13 c), which shows a DF-TEM image of the p-side that should have been covered, that the n-InP growth seem to have been seeded from the top i-InP layer. Even though the growth was not satisfactory in terms of masking and merging, improvements were made regarding the contact thickness and the shape of the masked area (Figure 4.13 a).

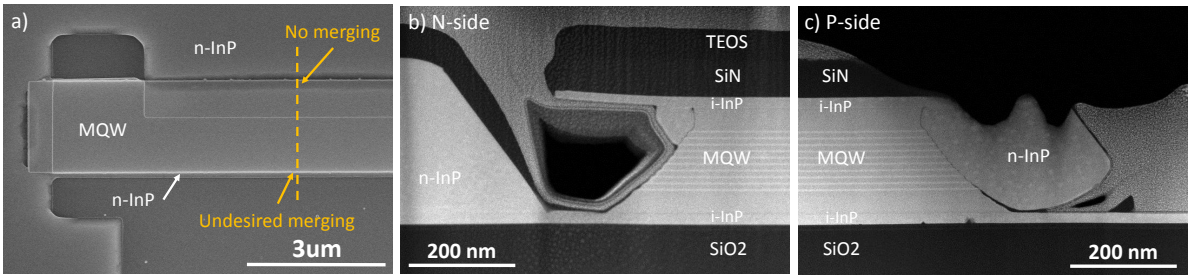

Figure 4.13: Images of a sample after n-InP contact regrowth where the surface preparation included 1 min HCl:H_2O (1:5 ratio) passivation and a 2 min rinse in DI water. a) Top view SEM image where the yellow line marks the place where the TEM lamella was cut. Cross-sectional DF-TEM images of different areas showing b) the n-side with insufficient merging and c) the p-side where growth was seeded by the top InP layer.

4.7 Summary of active devices

In this chapter, the rigorous development of the initial processes linked to the fabrication of the active lasers was shown. It appears essential to suppress the undercut by patterning the MQW stack by dry etching in the future. In this way, problems associated with TEOS masking and residues in the undercut could be avoided.

Chapter 5

Passive devices

Other components than the gain material such as Bragg reflectors, access waveguides and grating couplers are needed to construct a laser, as mentioned in section 2.1. Reflectors trap the light inside the material forming an optical cavity, access waveguides transfer the light out of the cavity and grating couplers diffract the light out of the sample. To ensure the performance of the passive components used in the active devices, test structures were fabricated to evaluate the design of the passive components. In blocks, key parameters for the different components were varied around simulated values.

Section 5.1 discusses the material choice and the fabrication of the passive devices. The characterization of the structures was performed by transmission measurements in a fiber optical measurement setup described in section 5.2. The principle theory of grating coupler design along with results from measurements on our grating coupler structures is presented in Section 5.3. The propagation losses in the access waveguides is determined in section 5.4 and a measured example of a Bragg reflector is shown in section 5.5.

5.1 Material choice and device fabrication

In order to avoid introducing new materials in our active devices, there are four possible materials to chose for the passive components: InAlGaAs MQW stack, intrinsic InP, n-doped InP and p-doped InP. The InAlGaAs MQW stack is a lossy material when not pumped and therefore not suitable. In the case of intrinsic InP, a third regrowth step needs to be added to the device fabrication processing flow which could add additional complexities. Using one of the doped InP materials for the passive components would only work in practice if the material absorption losses are reasonably low.

The absorption losses in a material, α [dB/cm], can be calculated according to [24]:

$$\alpha = \frac{k4\pi \log_{10}(e)}{10\lambda} \tag{5.1}$$

where k represents the extinction coefficient and λ the wavelength. Using the estimated extinction coefficients from Appendix C, a doping level of 1E19 cm^{-3} in the material would result in material losses of 66.3 dB/cm for n-doped InP and 563.9 dB/cm for p-doped InP. The n-doped losses are reasonably low and if an access waveguide has a length of for example 250 µm, this would result in approximately 1.6 dB of losses. Consequently, the n-doped InP was the material chosen for the passive components.

The samples were fabricated by growing a 235 nm thick n-InP layer with a doping level of about 1E19 cm^{-3} in the MOCVD. The material was bonded to the silicon oxide layer of a silicon substrate using the same DWB process as for the active devices, described in section 4.3. Once the donor wafer was removed, a 10 nm SiN hard mask was deposited by PECVD. The structures were written by EBL and the SiN hard mask was etched by RIE in CHF_3:O_2 for 20 sec and in SF_6:N_2 for 45 sec. Once the SiN hard mask was patterned, the n-InP layer was etched by inductively coupled plasma (ICP) etching for eight cycles.

5.2 Fiber optical measurement setup

The characterization of the passive components was performed using a fiber optical measurement setup illustrated in Figure 5.1. The principle behind the setup is to measure the transmitted light through a component by comparing the intensity of the light sent into the device with the light detected at the other end.

The setup consisted of a tunable laser light source connected to an optical fiber, a polarization controller, movable stages holding the optical probes, and a detector that sends the data to a spectrum analyzer, as shown in Figure 5.1. The setup was controlled through a LabView program by which automated measurements could be performed. Prior to the measurement of each device, an alignment procedure was conducted to find the position over the grating couplers where the transmission was maximized. Once the probes were aligned, the laser was swept between 1250-1370 nm and a transmission spectrum was recorded before moving to the next device and repeating the same procedure. All data analysis was made in Wolfram Mathematica.

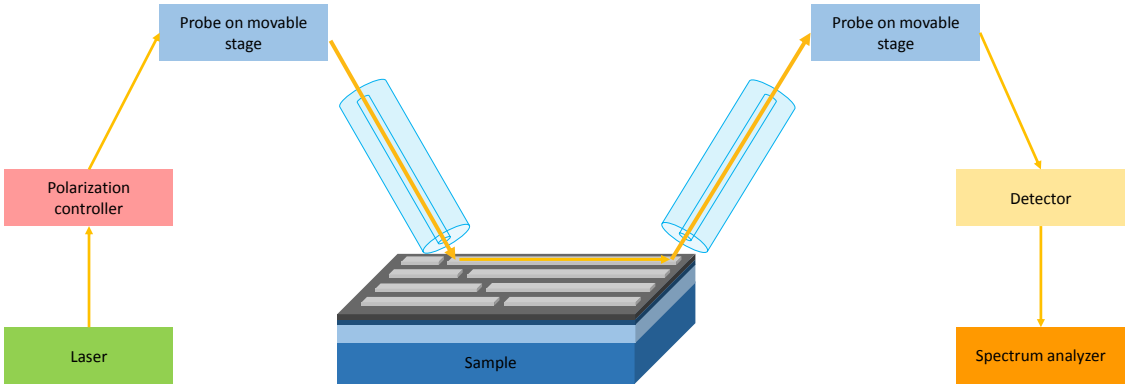

Figure 5.1: Schematic image of the fiber optical measurement setup used to measure transmission through a device. A light source is connected to an optical fiber which goes through a polarization controller before ending in an optical probe mounted on a movable stage. The light transmitted through the sample is coupled into a probe on the other side, the signal is detected and the data is sent to a spectrum analyzer.

5.3 Grating couplers

Measuring transmission through a waveguide requires efficient coupling of light from an external source between optical fibers and the waveguides. A grating coupler is a component which diffracts light out of plane from the sample and can be used to couple the light into or out of a waveguide. Due to its periodic structure, only light with certain wavelengths and incident angles can be coupled. A wide, tapered grating coupler is often used to focus light from a larger area into the waveguide, as shown in Figure 5.2 a). Parameters to consider when designing a grating coupler are the effective refractive index of the grating region n_{eff}, the central wavelength λ, the grating period Λ, the refractive index of the cladding material n_{clad}, the duty cycle or filling factor DC, and the angle between the surface normal and the incident light waves θ, see Figure 5.2. The parameters are related accordingly, as shown below [24]:

$$n_{eff} = \frac{\lambda}{\Lambda} + n_{clad} sin\theta \tag{5.2}$$

where

$$n_{eff} = n_{grat}^{eff} DC + n_{clad}^{eff}(1 - DC) \tag{5.3}$$

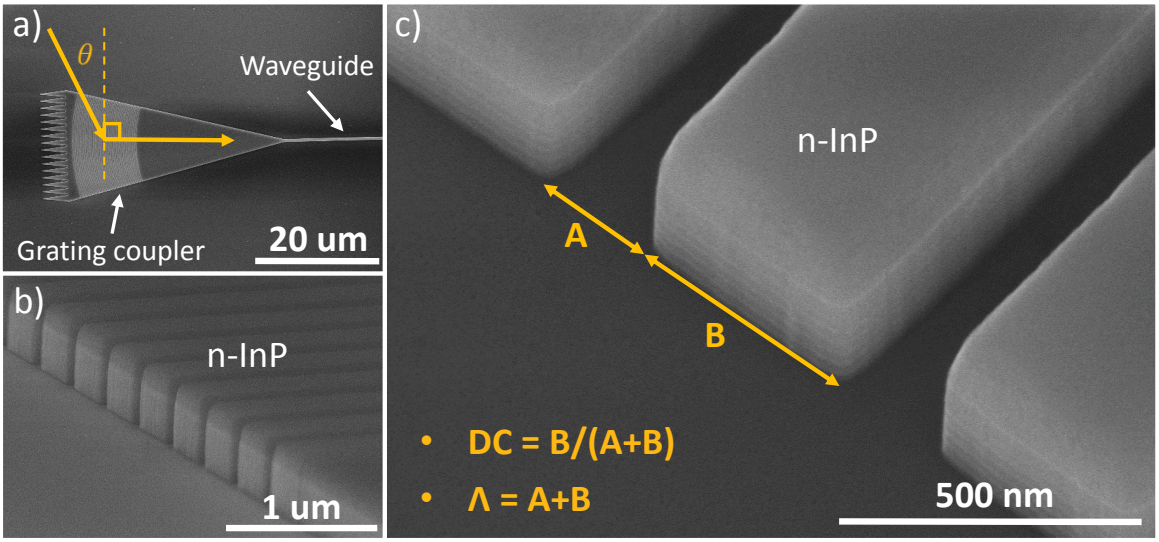

Figure 5.2: a) Top view SEM image of a grating coupler where the arrow represent the incident light beam and the angle θ. b) A tilted SEM image of the edge of a grating coupler. c) Tilted SEM image of grating coupler where the duty cycle, DC, and grating period, Λ, are explained.

A grating coupler can be designed to couple light of a certain polarization because the effective refractive indices of the TE and TM modes varies. Thus, it is possible couple light of for example the TE polarization and suppress light of the TM polarization.

The passive sample that was fabricated contained an array of grating couplers designed to couple light of the TE polarization with a SiO_2 cladding. The two grating couplers of each device were connected by 450nm wide and 200 µm long waveguide. The incident angle was set to 10 degrees and the central wavelength was assumed to be 1300 nm. For different duty cycles, the theoretical grating periods were calculated. For example, a DC of 0.8 would require a Λ of 610 nm.

The transmission was measured for devices with the same duty cycle of 0.8 but different grating coupler periods. The devices with grating periods around 610nm showed a distinct peak in the transmission for wavelengths that were around the central wavelength or slightly longer. An example of a transmission spectrum can be seen in Figure 5.3 where we have measured a device with a DC of 0.8 and grating period of 614nm. The central wavelength for this device is red-shifted for 10-15 nm which could be due the fact that the sample was measured without the SiO_2 cladding which effects the effective refractive index of the grating pair. In addition, the transmission was rather low even for the central wavelength, which could be due to the fact that the sample was not cleaned together with a narrow waveguide size, explained in more detail in the following section.

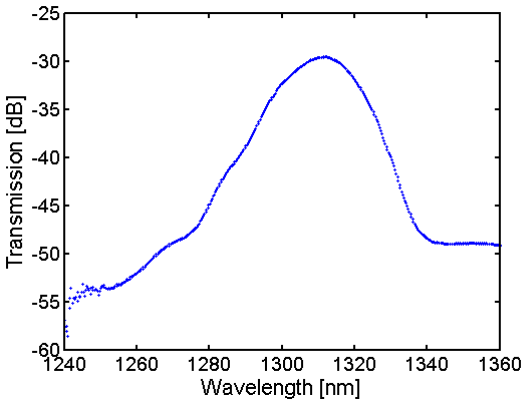

Figure 5.3: Transmission spectrum of a grating coupler device consisting of two grating couplers connected via a 200 µm long waveguide, both having a $DC = 0.8$ and a $\Lambda = 614nm$.

5.4 Access waveguides

To verify the estimated absorption values of 66 dB/cm for n-type InP, an evaluation of the propagation losses was conducted. Assuming that light decays when traveling through a waveguide due to absorption and scattering, the output intensity becomes proportional to the length of the waveguide, L. Plotting the maximum transmission for waveguides of various lengths gives a transmission-length dependency where the slope corresponds to the propagation losses and the intersection with the y-axis corresponds to the coupling losses, (Figure 5.4 a). To extract the maximum transmission for a specific waveguide, a Gaussian function was fitted to the obtained spectrum and the maximum value was recorded. Filters were used to exclude data with poor coupling or abnormal characteristics.

The structures were first measured without any treatment after the ICP etch. The variation in propagation losses between the 450 nm wide and 10 µm wide waveguides was more than 200 dB/cm, see blue data in Figure 5.4 b). In a wide waveguide, the propagation losses are dominated by absorption but as the waveguides becomes narrower, the propagation losses could instead be dominated by scattering if the side walls are rough. The large difference in losses between the narrow and the wide waveguides indicated that the structures had rough side walls which was also confirmed by SEM. Figure 5.5 a) shows a SEM image of a part of a grating coupler with no treatment where the arrows indicate the presence of particles and rough side walls (the lateral stripes).

An attempt to reduce the side wall roughness was conducted by immersing the sample in a solution of H_3PO_4:H_2O (1:10) for 1 min. From Figure 5.5 b) it can be seen that the amount of remained particles is less (compared to Figure 5.5 a) while the no clear

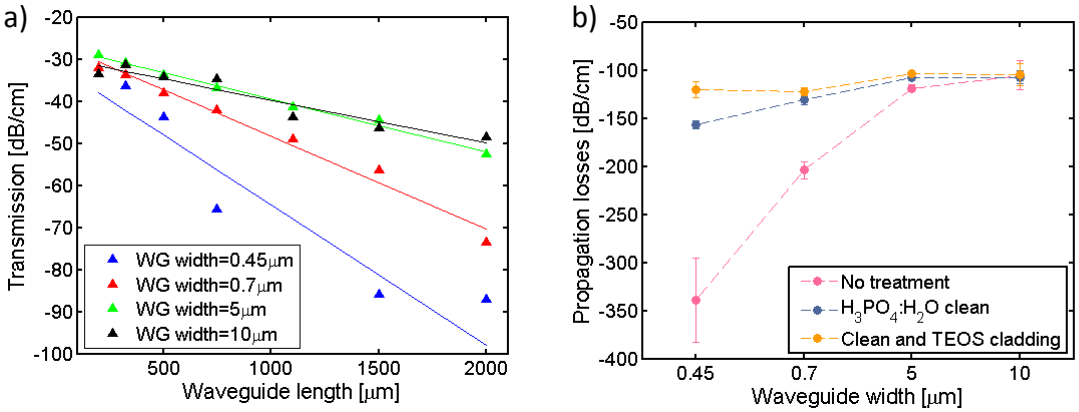

Figure 5.4: a) Graph of the transmission versus waveguide length L, measured for four different waveguide widths. The sample was measured without any surface treatment. A steeper slope indicates higher propagation losses. b) Graph of the propagation losses versus waveguide width for three different sample conditions; no treatment, sample cleaned in H_3PO_4:H_2O (1:10) and sample cleaned with a 1.5 µm TEOS cladding.

difference regarding the lateral stripes can be seen. It is likely that the particles consisted of an In-containing oxide and could therefore be removed by the chemical treatment. The striped lines correlate with the number of etch cycles performed inside ICP which indicates that they were formed in the material during the ICP process. The lateral stripes can change the mode profile but because the lines are consistent along the waveguide also the mode profile will also be consistent in the direction of propagation and therefore only have a minor influence on the losses. The red data points in Figure 5.4 b) shows that the losses were significantly reduced after the H_3PO_4:H_2O treatment and even more for the sample with 1.5 µm TEOS cladding where no pronounced difference in losses between the various waveguide widths could be seen from the green data points in Figure 5.4 b). It was concluded that the propagation losses, including absorption and scattering, were around 100 dB/cm. The value is less than a factor two off from the estimated material absorption loss of 66.3 dB/cm which confirmed that our estimate value was in the correct range. The difference could be due to the side wall roughness or the fact that the doping level could potentially be higher than the targeted value of 1E19cm^{-3}.

5.5 Distributed Bragg Reflectors

Reflectors are needed to form an optical cavity, as mentioned in Section 2.1.2. The idea is to create a mirror at the end of the gain material to reflect the light back to form a standing wave inside the cavity, as shown in Figure 5.6 a). As explained in section 2.1.2, the mirror

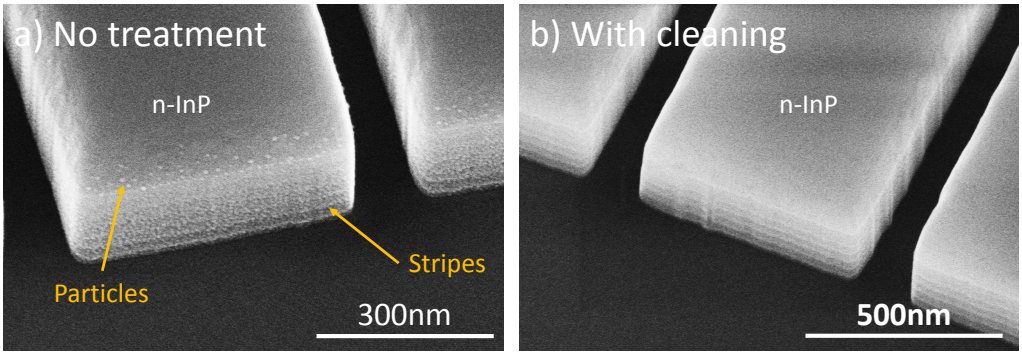

Figure 5.5: Images show a part of the grating coupler a) prior to any treatment and b) after 1 min H_3PO_4:H_2O (1:10) clean.

consist of a periodic structure of two different refractive index materials where only the light of wavelengths close to the Bragg wavelength can be reflected back and interfere constructively. Measuring transmission through a component with Bragg reflectors will produce a spectrum with a drastic decrease in the transmitted light around the Bragg wavelength.

An array of DBR structures, which were connected by a 450 nm wide and 300 µm long waveguides, were fabricated on a passive n-doped InP sample. The devices were designed to reflect TE polarized light (based on the same principle as explained in Section 5.3) and have a SiO_2 cladding. On the sample, parameters such as duty cycle, grating period and number of grating pairs were swept. Given the central wavelength of 1300 nm and a duty cycle of 0.6, the theoretical grating period was calculated to 350 nm. Figure 5.6 b) shows the transmission spectrum for a measured device with a duty cycle of 0.5, a grating period of 367 nm and 41 grating pairs. The transmission spectrum displays a nearly 40 dB attenuation for wavelengths below 1330 nm, indicating a photonic bandgap induced by the Bragg reflections. Because the transmission in Figure 5.6 was measured for wavelengths between 1250-1380 nm it was not possible to determine the bandwidth of the photonic bandgap. Additionally, because the transmitted and not reflected light was measured it is not possible to confirm that the light was actually reflected straight back. In fact, the light could also have been reflected out of plane from the sample. If this was the case, an efficient resonant cavity would not form and the probability to reach a lasing mode would decrease drastically. Measurements of the reflected light for a larger spectral range should be conducted to confirm the performance of the Bragg reflectors.

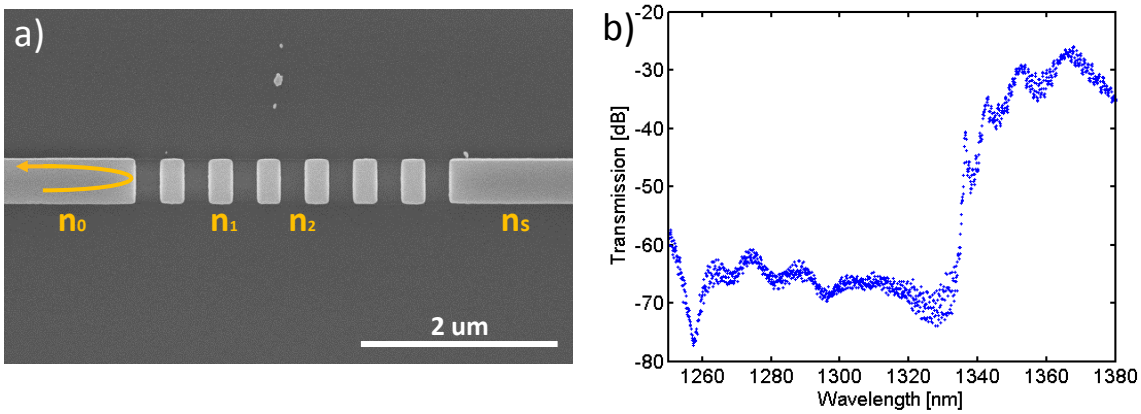

Figure 5.6: a) Top view SEM image of Bragg reflector with six alternating index pairs. b) Transmission spectrum of a DBR device with a DC of 0.5 and a grating period of 367 nm.

5.6 Summary of passive devices

In this chapter, the passive components of the laser i. e. the grating couplers, the access waveguides and the Bragg reflectors were fabricated and investigated. Through transmission measurements conducted in a fiber optical measurement setup, it was concluded that the material losses were approximately 100 dB/cm. A grating couper structure with a duty cycle of 0.8 and a grating period of 610 nm can be used to efficiently diffract light in and out of the devices on our sample. A "Bragg reflector like" behaviour was shown for a device with a duty cycle of 0.6 and a grating period of 367 nm. However, further measurements should be conduted in order to confirm the performance of the Bragg reflectors.

Chapter 6

Conclusion and outlook

This work present an attempt to design and fabricate a lateral current injection (LCI) laser integrated on silicon. The laser is required to have an ultra-low power consumption and the possibility to be three dimensionally integrated on IBM's silicon photonics platform. The laser threshold current is proportional to the overlap between the optical mode and the gain material. In order to minimize the threshold current and power consumption of our lasers, the parameter space was analyzed through optical simulations. In addition to the optical simulations, the passive components of the laser, i.e. grating couplers, access waveguides and Bragg reflectors, were fabricated and analyzed to ensure their performance before being processed on the active devices.

Based on the optical simulation results, suitable designs for the active LCI lasers were chosen to be experimentally fabricated. The rather complex fabrication process was started by developing a recipe for growing the optical gain material. The gain material was an epitaxial multiquantum well (MQW) stack of consisting of 10 InAlGaAs quantum wells with an emission peak at 1288nm. The MQW stack was successfully integrated on a silicon oxide wafer through direct wafer bonding. A wet etch process for the patterning of the gain material as well as processes to mask areas for selective epitaxial regrowth were developed. Regrowth experiments concluded that the surface preparation of the sample is of essential importance for obtaining a high quality InP contacts and also for the lateral merging with the gain material. Through a meticulous LCI laser process development, a solid base is established from which the project can continue.

After six months of working with the realization of a LCI laser integrated on silicon I have come to the understanding that the "to-do"-list will never be completed but instead be continuously get refilled with new ideas and concepts. However, as a guidance for the interested reader I have listed a few points that I would address primarily if I was to continue the project:

- Measure the intensity of the reflected light on the passive Bragg mirror devices to ensure that the light is actually reflected straight back and not out of plane.
- Finish the last steps in the fabrication process of the active devices. Once the devices are complete, performing electro-optical measurements would reveal if the structures will lase or not and under which pumping conditions.
- Develop a dry etch process for the patterning of the gain material. If straight side walls could be achieved instead of the undercut created by the wet etching process, the troublesome masking and unmasking of the undercut could be avoided. The process would also become more robust and not dependent on human errors occurring from inaccurate mixing of chemicals and etch times. Additionally, the structures would correlate with the simulations to a higher degree.
- Investigate the regrowth process and contact merging thoroughly to understand what surface properties are required to achieve satisfactory and reproducible results.
- Adapt the concept to a gain material consisting of quantum dots instead of quantum wells. It is believed that quantum dot lasers can operate at higher temperatures which allows for a higher pumping power to be used, resulting in an increase in optical output power.

Appendix A

The laser rate equations

The laser rate equations [22]:

$$\frac{dN}{dt} = \frac{n_i I}{qV_{QW}} - \frac{N}{\tau_r} - \frac{N}{\tau_{nr}} - v_g g_0 log\left(\frac{N}{N_{tr}}\right) N_p$$

$$\frac{dN_p}{dt} = \Gamma v_g g_0 log\left(\frac{N}{N_{tr}}\right) N_p - \frac{N_p}{N_{tr}} - \Gamma\beta\frac{N}{\tau_r}$$

In the steady state regime, $dN/dt=0$ and $dN_p/dt=0$.

$\boldsymbol{N}$ - carrier density
$\boldsymbol{n_i}$ - carrier injection efficiency
$\boldsymbol{I}$ - current
$\boldsymbol{q}$ - carrier charge
$\boldsymbol{V_{QW}}$ - volume of active region
$\boldsymbol{\tau_r}$ - radiative carrier lifetime
$\boldsymbol{\tau_{nr}}$ - nonradiative carrier lifetime
$\boldsymbol{v_g}$ - waveguide group velocity
$\boldsymbol{g_0}$ - material gain factor
$\boldsymbol{N_{tr}}$ - carrier density at transparency
$\boldsymbol{N_P}$ - photon density
$\boldsymbol{\Gamma}$ - modal confinement factor
$\boldsymbol{\beta}$ - material dependent parameter

Maxwell's equations of electromagnetism [25]:

$$\nabla \cdot \mathbf{B} = 0$$
$$\nabla \times \mathbf{E} = -\frac{\partial \mathbf{B}}{\partial t}$$
$$\nabla \cdot \mathbf{D} = \rho$$
$$\nabla \times \mathbf{H} = \mathbf{J} + \frac{\partial \mathbf{D}}{\partial t}$$

where $\mathbf{B}$ is the magnetic induction field, $\mathbf{E}$ is the electric field, $\mathbf{D}$ is the electric displacement field, $\mathbf{H}$ is the magnetic field and ρ and $\mathbf{J}$ are electric charge and current densities.

Appendix B

Hall Effect Measurements

Hall effect measurements can be used to determine both the mobility μ and carrier concentration n of a semiconducting material. When a current is applied between two transverse nodes in a sample, charge carriers flow straight between the nodes. If a magnetic field is simultaneously applied perpendicular to the current, the charge carriers are forced to deviate from their straight path and instead they are accumulated on one side. As a result, the charge distribution is non-uniform across the sample giving rise to an electrical field [32]. This potential difference is known as the Hall voltage V_H and can be measured as shown in Figure B.1 a).

Once V_H is measured, the hall mobility μ_H, can be calculated:

$$\mu_H = \frac{|V_H|t}{BI\rho}$$

Where t is the thickness of the sample, B is the magnetic field, I is the current and ρ is the resistivity. To obtain accurate results, the resistivity of the sample ρ, should be determined by a Van Der Pauw measurement technique. The technique is similar to the measurement of the hall voltage, the difference is that the current is applied between adjacent nodes and measured on the opposite adjacent nodes. This measurement is performed multiple times between different adjacent nodes resulting in an average resistivity of the sample [33].

Given the hall mobility μ_H, the resistivity ρ and the carrier charge q, the carrier concentration could be calculated though this relation:

$$\rho = \frac{1}{qn\mu_H}$$

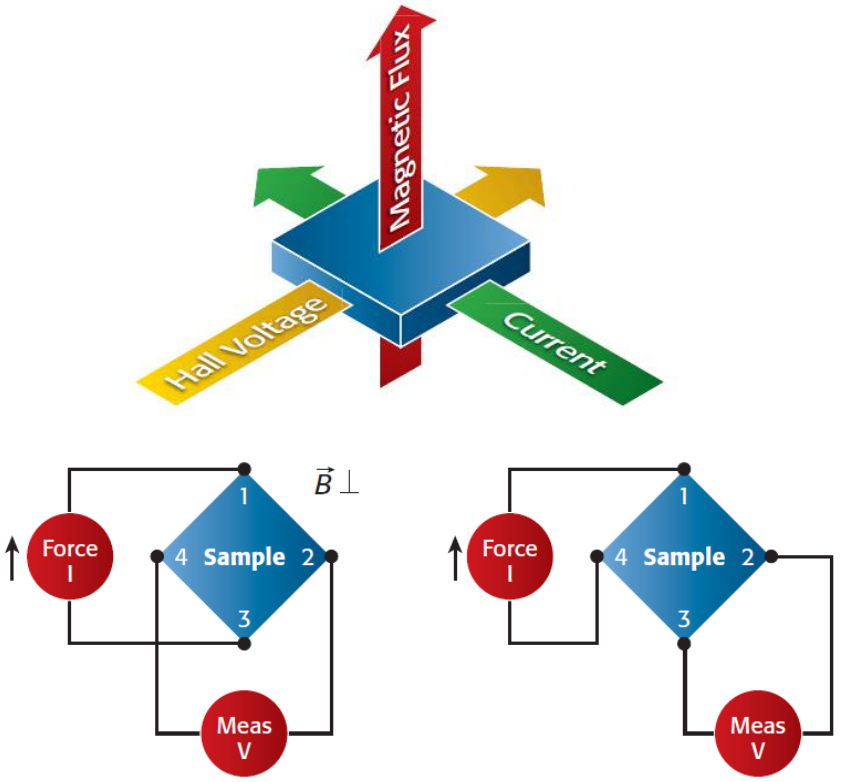

a) Hall voltage measurement b) Van der Pauw resistance measurement

Figure B.1: Illustration of the Hall effect where measurements of a) the Hall voltage and b) van der Pauw resistance are shown [32].

Appendix C

Complex effective refractive index model

In Section 3.1.3 the absorption losses were investigated by varying the doping level of n- and p-doped InP. As mentioned the losses depend on the imaginary part of the complex refractive index, $\underline{n}$. The complex refractive index is related its complex relative dielectric constant and can be derived from Maxwell's equations [25]:

$$\underline{n} = \sqrt{\underline{\varepsilon}}$$

The complex refractive index of a material $\underline{n}$ is linked to the complex relative dielectric constant $\underline{\varepsilon}$ through the following relation:

$$\underline{\varepsilon} = \varepsilon' + i\varepsilon'' = \underline{n}^2 = (n + i\kappa)^2$$

Their components are in their turn related by:

$$\varepsilon' = n^2 - \kappa^2$$

$$\varepsilon'' = 2n\kappa$$

and

$$n = \sqrt{\frac{|\,\underline{\varepsilon}\,| + \varepsilon'}{2}}$$

$$\kappa = \sqrt{\frac{|\,\underline{\varepsilon}\,| - \varepsilon'}{2}}$$

where

$$| \underline{\varepsilon} | = \sqrt{\varepsilon'^2 + \varepsilon''^2}$$

A former IBM colleague had collected data of how the components of the complex relative dielectric function in n- and p-type InP vary with the doping level at at fixed wavelength of 1300nm [27–29, 34]. Based on this information, a model was constructed which included a fourth order polynomial fit to the data points.

$$f(x) = a_0 + a_1 x + a_2 x^2 + a_3 x^3 + a_4 x^4$$

where the parameters obtained from the polynomial fit are listed in the table below:

	n-type		p-type	
	ε'	ε"	ε'	ε"
a_0	10.26670933328	0	10.266709331587	0
a_1	-2.0223730969577E-020	1.0128300116287E-022	-3.6113805486617E-021	8.613106248603E-022
a_2	9.9594225232293E-042	-9.9757098611064E-044	2.9957554397881E-043	-1.5149970773843E-043
a_3	-5.9828233063736E-066	3.1500515754869E-068	-1.1045380901421E-066	2.6257307505549E-067
a_4	3.344797676039E-086	-1.7443998098148E-088	6.2065115172485E-087	-1.4698869342026E-087

Table C.1: Fitting parameters for the complex relative dielectric function for n- and p-typ InP.

Finally, the ordinary refractive index n, and the extinction coefficient k, in InP could be calculated for different n- and p-doping levels, see figure C.

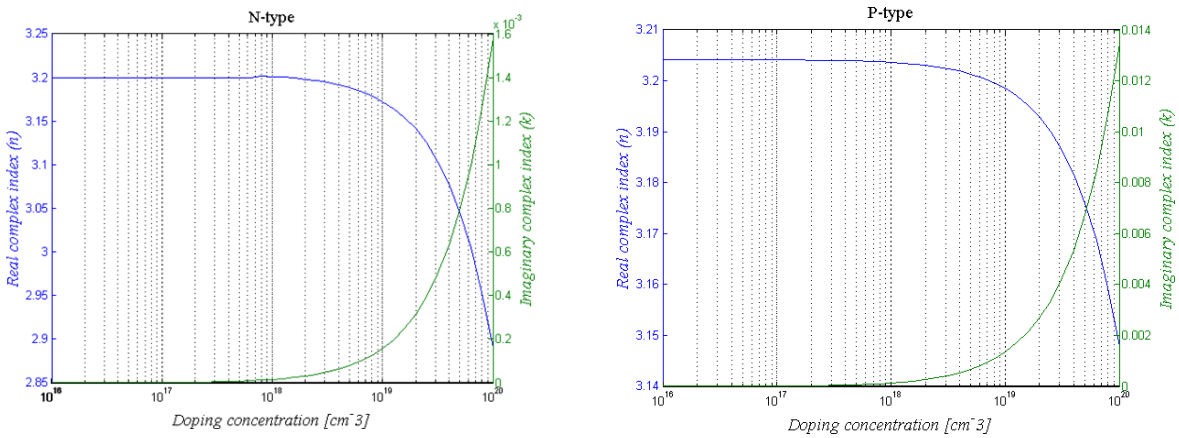

Figure C.1: The ordinary refractive index, n, and the extinction coefficient, k, versus doping level in a) n-type InP and b) p-type InP.

Acknowledgements

First, I would like to thank Dr. Walter Reiss, Dr. Heike Riel and Dr. Jean Fompeyrine for giving me the opportunity to write my master thesis in the Materials Integration and Nanoscale Devices (MIND) team at IBM Research Zurich. It has truly been a great experience working amongst such passionate and welcoming people. Furthermore, I would like to address specical thanks

To Dr. Sepideh Gorji Ghalamestani, my supervisor at Lund University, for your support throughout the project. Your knowledge in writing scientific reports along with your big effort to help me make the most of my thesis has been of great importance to me.

To Dr. Lukas Czornomaz, my supervisor at IBM. Your seemingly endless knowledge about III-V integration on silicon and device fabrication together with your eagerness to see the project succeed has been invaluable. Your enthusiastic and encouraging persona has made it a true pleasure to work with you.

To Dr. Stefan Abel, my co-supervisor at IBM, for your help with teaching me about optical simulations and measurements and for your contribution to the mask designs.

To Dr. Charles Caer, for interesting discussions on laser designs and for your contribution with model of the laser performance estimation and to the mask designs.

To Dr. Vladimir Djara, for all the time spent in the cleanroom and for teaching me how to systematically perform laboratory experiments.

To Marilyne Sousa, for your helpfulness and effort in performing the TEM analysis.

To Svenja, Johanna, Viola, Youri and Felix for daily sunshine and for always having time to discuss my experiments and results.

References

[1] R. Anderson, "Data processing in the internet of things - the move from pipedream to reality." [Online]. Available: http://ieeexplore.ieee.org/xpls/abs_all.jsp?arnumber=124191&tag=1

[2] D. A. B. Miller and H. M. Özaktas, "Limit ot the Bit-Rate Capacity of Electrical Interconnects from the Aspect Ratio of the System Architecture," *Journal od Parallel and Distributed Computing*, vol. 41, no. 1, pp. 42–52, Feb. 1997. [Online]. Available: http://www.sciencedirect.com/science/article/pii/S074373159691285X

[3] L. T. Hwang and I. Turlik, "A Review of the Skin Effect as Applied to Thin Film Interconnections," *IEEE Transactiond on Components, Gybrids, and Manufacturing Technology*, vol. 15, no. 1, pp. 43–55, Feb. 1992. [Online]. Available: http://ieeexplore.ieee.org/xpls/abs_all.jsp?arnumber=124191&tag=1

[4] D. A. B. Miller, "Rationale and Challenges for Optical Interconnects to Electronic Chips," *Proceedings of the IEEE*, vol. 88, no. 6, pp. 728–749, Jun. 2000. [Online]. Available: http://ieeexplore.ieee.org/xpls/abs_all.jsp?arnumber=867687&tag=1

[5] D. Miller, "Device Requirements for Optical Interconnects to CMOS Silicon Chips," *Integrated Photonics Research, Silicon and Nanophotonics in Switching*, p. PMB3, Jul. 2010. [Online]. Available: http://ieeexplore.ieee.org/xpls/abs_all.jsp?arnumber=867687&tag=1

[6] B. E. A. Saleh and C. M. Teich, *Fundamentals of Photonics.* New York: Wiley, 1991.

[7] L. Chrostowski and M. Hochberg, *Silicon Photonics Design - From Devices to Systems.* Cambridge University Press, 2015.

[8] H. Rong, A. Liu, R. Jones, O. Cohen, D. Hak, R. Nicolaescu, A. Fang, and M. Paniccia, "An all-silicon Raman Laser," *Nature*, vol. 433, pp. 292–294, Jan. 2005. [Online]. Available: http://www.nature.com/nature/journal/v433/n7023/full/nature03273.html

[9] H. Rong, R. Jones, A. Liu, O. Cohen, D. Hak, A. Fang, and M. Paniccia, "A continous-wave Raman silicon laser," *Nature*, vol. 433, no. 1, pp. 725–728, Jan. 2005. [Online]. Available: http://www.nature.com/nature/journal/v433/n7027/full/nature03346.html

[10] R. Soref, "The Past, Present, and Future of Silicon Photonics," *IEEE Journal of Selected Topics in Quantum Electronics*, vol. 12, no. 6, pp. 1678–1687, Nov. 2007. [Online]. Available: http://ieeexplore.ieee.org/xpls/abs_all.jsp?arnumber=4032698

[11] T. Okamura, M. Kurokawa, M. Shirao, D. Kondo, H. Ito, N. Nishiyama, T. Maruyama, and S. Arai, "Lateral current injection GaInAsP/InP laser of semi-insulating substrate for membrane-based photonic circuits," *Optics Express*, vol. 17, no. 15, pp. 12 564–12 570, 2009. [Online]. Available: https://www.osapublishing.org/oe/abstract.cfm?uri=oe-17-15-12564

[12] A. W. Fang, H. Park, O. Cohen, R. Jones, M. J. Paniccia, and J. E. Bowers, "Electrically pumped hybrid AlGaInAs-silicon evanescent laser," *Optics Express*, vol. 14, no. 20, pp. 9203–9210, 2006. [Online]. Available: https://www.osapublishing.org/oe/abstract.cfm?uri=oe-14-20-9203

[13] Y. Takahashi, Y. Inui, M. Chihara, T. Asano, R. Terawaki, and S. Noda, "A micrometer-scale Raman silicon laser with a microwatt threshold," *Nature*, vol. 498, pp. 470–474, 2013. [Online]. Available: http://www.nature.com/nature/journal/v498/n7455/abs/nature12237.html

[14] A. Furuya, M. Makiuchi, O. Wada, and T. Fujii, "AlGaAs/GaAs Lateral Current Injection Multiquantum Well (LCI-MQW) Laser Using Impurity-Induced Disordering," *Journal of Quantum Electronics*, vol. 24, no. 12, pp. 2448–2453, Dec. 1988.

[15] E. T. H. Sargent, G. Tan, and J. M. Xu, "Lateral Current Injection Lasers: Underlying Mechanisms and Design for Improved High-Power Efficiency," *Journal of Lightwave technology*, vol. 16, no. 10, Oct. 1998. [Online]. Available: http://ieeexplore.ieee.org/xpl/abstractAuthors.jsp?arnumber=721073

[16] W. T. Tsang, "Extremely low threshold (AlGa) As modified multiquantum well heterostructure lasers grown by molecular-beam epitaxy," *Applied Physics Letters*, vol. 39, no. 10, pp. 786–788, Nov. 1981. [Online]. Available: http://scitation.aip.org/content/aip/journal/apl/39/10/10.1063/1.92583;jsessionid=2fgqefigl7mb2.x-aip-live-03

[17] K. Doi, J. Shindo, T. abd Lee, T. Amemiya, N. Nishiyama, and S. Arai, "Thermal Analysis of Lateral-Current-Injection Membrane Distributed Feedback Laser," *Journal of Quantum Electronics*, vol. 50, no. 5, pp. 321–326, May 2014. [Online]. Available: http://ieeexplore.ieee.org/stamp/stamp.jsp?arnumber=6756972

[18] L. Czornomaz and J. Fompeyrine, "Semiconductor structure and method for manufacturing a semiconductor structure," Patent.

[19] M. Futami, T. Shindo, T. Koguchi, K. Shinno, T. Amemiya, N. Nishiyama, and S. Arai, "GaInAsP/InP Lateral Current Injection Laser with Uniformly Distributed Quantum-Well Structure," *IEEE Photonics Technology Letters*, vol. 24, no. 11, pp. 888–890, Jun. 2012. [Online]. Available: http://ieeexplore.ieee.org/xpls/abs_all.jsp?arnumber=6179305

[20] J. Piprek, J. K. White, and A. J. Spring Thorpe, "What limits the maximum Output Power of Long-Wavelength AlGaInAs/InP Laser Diodes?" *Journal of Quantum Electronics*, vol. 38, no. 9, pp. 1253–1259, Sep. 2002. [Online]. Available: http://ieeexplore.ieee.org/stamp/stamp.jsp?tp=&arnumber=1027769

[21] J. Hofrichter, "Inp microdisks for optical signal processing and data transmission," Ph.D. dissertation, Technische Universitat Endhoven, 2012. [Online]. Available: https://pure.tue.nl/ws/files/3603335/750668.pdf

[22] C. L. A, S. W. Corzine, and M. L. Mashanovitch, *Diode lasers and photonic integrated circuits*. New York: Wiley, 2012.

[23] R. G. Hunsperger, *Integrated Optics - Theory and Technology*. New York: Springer, 2009.

[24] L. Chrostowski and M. Hochberg, *Silicon Photonics Design*. Cambridge: Cambridge University Press, 2015.

[25] M. Fox, *Optical Properties of Solids*. Oxford: Oxford University press, 2010.

[26] D. Melati, A. Melloni, and F. Morichetti, "Real photonic waveguides: guiding light through imperfections," *Advances in Optics and Photonics*, vol. 6, no. 2, pp. 156–224, May 2014. [Online]. Available: https://www.osapublishing.org/aop/abstract.cfm?uri=aop-6-2-156

[27] L. Chusseau, P. Martin, C. Brasseur, C. Alibert, P. Herve, F. Lozes-Duput, and E. K. V. Rao, "Carrier-induced change due to doping in refractive index of InP: Measurements at 1.3 and 1.5 um," *Applied Physics Letters*, vol. 69, no. 20, pp. 3053–3056, Nov. 1996. [Online]. Available: http://scitation.aip.org/content/aip/journal/apl/69/20/10.1063/1.116837

[28] M. Bugajski and W. Lewanndowski, "Concentration-dependent absorption and photoluminescence of n-type InP," *Applied Physics Letters*, vol. 57, no. 2,

pp. 521–530, Jan. 1985. [Online]. Available: http://scitation.aip.org/content/aip/journal/jap/57/2/10.1063/1.334786

[29] H. C. Casey and P. L. Carter, "Variation of intervalence band absorption with hole concentration in p-type InP," *Applied Physics Letters*, vol. 44, no. 1, pp. 82–83, Jan. 1984. [Online]. Available: http://scitation.aip.org/content/aip/journal/apl/44/1/10.1063/1.94561

[30] L. Czornomaz, N. Daix, D. Caimi, M. Sousa, R. Erni, M. D. Rossell, M. El-Kazzi, C. Rossel, C. Marchiori, E. Uccelli, M. Richter, H. Sieqwart, and J. Fompeyrine, "An integration path for gate-first utb iii-v-on-insulator mosfets with silicon, using direct wafer bonding and donor wafer recycling," *Electron Devices Meeting*, pp. 23.4.1–23.4.4, Dec. 2012. [Online]. Available: http://ieeexplore.ieee.org/xpls/abs_all.jsp?arnumber=6479088&tag=1

[31] A. J. D. Alfonso, B. Freitag, D. Klenov, and L. J. Allen, "Atomic-resolution chemical mapping using energy-dispersive x-ray spectroscopy," *Physical Review B*, vol. 81, no. 10, 2010. [Online]. Available: http://journals.aps.org/prb/pdf/10.1103/PhysRevB.81.100101

[32] R. Green, "White paper: Hall Effect Measurements in Materials Characterization," *Keithley Instruments Inc.*, 2011. [Online]. Available: http://mrmackenzie.wikispaces.com/file/view/HallEffect_WhtPapr.pdf

[33] L. J. Van Der Pauw, "A method of measuring the resistivity and Hall coefficient on lamellae of arbitrary shape," *Philips Technical Review*, vol. 20, pp. 220–224, 2958. [Online]. Available: http://aki.issp.u-tokyo.ac.jp/okano/WalWiki/etc/VDP_PTR_20_220.pdf

[34] B. Bennet, R. Soref, and J. A. Del Alamo, "Carrier-induced change in refractive index of InP, GaAs and InGaAsP," *IEEE Journal of Quantum Electronics*, vol. 26, no. 1, pp. 113–122, Jan. 1990. [Online]. Available: http://ieeexplore.ieee.org/xpls/abs_all.jsp?arnumber=44924&tag=1